FY 07 Annual Report, MURI Award N00014-04-1-0599 Friction and Wear Sciences for a Highly Durable Railgun Weapon

C. Persad and S. Satapathy

Institute for Advanced Technology
The University of Texas at Austin

October 2007

IAT.R 0512

Institute for Advanced Technology
The University of Texas at Austin

IAT

REPORT DOCUMENTATION PAGE

Form Approved
OMB NO. 0704-0188

1. AGENCY USE ONLY (Leave blank)	2. REPORT DATE October 2007	3. REPORT TYPE AND DATES COVERED Annual Report, FY07

4. TITLE AND SUBTITLE	5. FUNDING NUMBERS
FY 07 Annual Report, MURI Award N00014-04-1-0599 Friction and Wear Sciences for a Highly Durable Railgun Weapon	Contract # N00014-04-1-0599

6. AUTHOR(S)

C. Persad and S. Satapathy

7. PERFORMING ORGANIZATION NAME(S) AND ADDRESS(ES)	8. PERFORMING ORGANIZATION REPORT NUMBER
Institute for Advanced Technology The University of Texas at Austin 3925 W. Braker Lane, Suite 400 Austin, TX 78759-5316	IAT.R 0512

9. SPONSORING / MONITORING AGENCY NAME(S) AND ADDRESS(ES)	10. SPONSORING / MONITORING AGENCY REPORT NUMBER
Office of Naval Research Regional Office San Diego 4520 Executive Drive STE 300 San Diego CA 92121-3019	

11. SUPPLEMENTARY NOTES

12a. DISTRIBUTION / AVAILABILITY STATEMENT	12b. DISTRIBUTION CODE
Approved for public release; distribution unlimited.	A

13. ABSTRACT *(Maximum 200 words)*

The interior ballistics of multi-shot electromagnetic launchers are more complex than that of conventional propellant guns. To be effective, a weapon must be able to fire thousands of rounds without refurbishment. New approaches are needed to understand the friction and wear sciences that influence the life of the railgun bore. A coordinated series of experimental measurements and analytical frameworks are required in order to produce a robust method of predicting the life of a railgun barrel given its design and mission. Specific tasks were: 1) investigate the physical and chemical interactions and processes that occur at the sliding electrical contact interface; 2) determine the parameters that control the life of rails in a railgun; and 3) design, develop, and test functional materials for rail wear control. Selected results are summarized here.

14. SUBJECT TERMS Sliding electrical contact interface, rail life, wear, materials			15. NUMBER OF PAGES 63
			16. PRICE CODE

17. SECURITY CLASSIFICATION OF REPORT Unclassified	18. SECURITY CLASSIFICATION OF THIS PAGE Unclassified	19. SECURITY CLASSIFICATION OF ABSTRACT Unclassified	20. LIMITATION OF ABSTRACT UL

Fiscal Year 2007 Annual Report: N00014-04-1-0599

Last Modified: 7/21/2007 6:18:36 PM

Name: Chadee Persad

Organization: THE UNIVERSITY OF TEXAS AT AUSTIN

City/State/Country: Austin/TX/USA

Title: Senior Scientist

Zip Code: 78713-7726

Phone: (512) 232-4492

Fax: (512) 471-9096

Email: chadee_persad@iat.utexas.edu

Contract Information

Contract/Grant Number: N00014-04-1-0599

Contract/Grant Title: Friction and Wear Sciences for a Highly Durable Railgun Weapon

Program Officer: Peter Schmidt

CO-PI Information

Number of Co-PIs: 1

Co-Investigator # 1

Name: Sikhanda Satapathy

Organization: Institute for Advanced Technology

City/State/Country: Austin/TX/

Title: Research Scientist

Zip Code: 78759

Phone: (512) 232-4455

Fax: (512) 471-9096

Email: sikhanda@iat.utexas.edu

Abstract

The interior ballistics of multi-shot electromagnetic launchers are more complex than that of cannons that use conventional propellants. Railguns are one class of electromagnetic launcher that have near-term potential for use as a weapon on an electric ship. To be effective such a weapon must be able to fire thousands of rounds without refurbishment. New approaches are needed to understand the friction and wear sciences that influence the life of the bore of a railgun. A coordinated series of experimental measurements and analytical frameworks are required in order to produce a robust method of predicting the life of a railgun barrel given its design and mission. Specific tasks were: 1) investigate the physical and chemical interactions and processes that occur at the sliding electrical contact interface; 2) determine the parameters that control the life of rails in a railgun; and 3) design, develop, and test functional materials for rail wear control. Selected results are summarized here. University researchers at The University of Texas at Austin (UT), Northwestern University (NU), and the Naval Postgraduate School (NPS), as well as Navy professionals and students at the US Naval Academy (USNA), the Navy Research Laboratories (NRL), and the Naval Surface Warfare Center (NAVSEA), are collaborating in this work.

Technical Section

N00014-04-1-0599.doc

Technology Transfer

The technology transfer from the Navy ONR Railgun Tribology MURI at The University of Texas started with the teaming arrangements that included personnel from the Naval Research Laboratory (NRL) and the Army Research Laboratory (ARL). Since then, there has been an expanded effort to draw upon faculty and students at the US Naval Academy (USNA) and the Naval Postgraduate School (NPS). A close working relationship has developed with the Metal Matrix Composites group at NAVSEA Carderock stemming from a mutual interest in graded materials for tribological applications. The paragraphs below provide a description of some of the types of interactions that have initiated and facilitated the continuing technology transfer process. Industry Interactions The Navy ONR hosted a technology transfer day at IAT, Austin, TX. The Railgun Tribology work performed under this MURI Program was briefed to the invitees. On Jan 24-26, 2006 ONR (Roger Ellis, EM Railgun INP, Office of Naval Research) hosted the technology transfer day at IAT. The purpose was to update three of the Navy's new industry partners regarding the state of the art in railgun bore life development. The industry partners are in the process of designing a 32MJ demonstration launcher for the Navy facility at Dahlgren, VA. There have been a series of visits and continuing technical interactions with these industry teams over the last eighteen months. Navy Faculty & Student Interactions Aluminum-silicon carbide metal-matrix composite materials that were cast by NSWC Carderock were tested on an IAT laboratory launcher as a rail insert. Samples of similar materials were distributed for railgun test and evaluation under the joint efforts of NSWC Carderock (Divecha), NRL (Meger), GA Tech (Danyluk), and UT-IAT (Persad). Persad worked with Commander Brown and his student at the USNA - Lt. Joseph Koessler - to report this work at the Navy-sponsored classified EML Symposium held in Washington DC in May 2007. Lt. Joseph Koessler is pursuing studies at The Naval Postgraduate School. MURI Teams Research Reviews and Cooperative Research- Our semi-annual reviews have been held at Austin, TX., Evanston, IL., Arlington, VA., and in Atlanta, GA. These meetings, which are attended by Navy engineers and scientists, feature technical presentations by the MURI faculty investigators from The University of Texas at Austin, The Naval Postgraduate School, and Northwestern University. CD compilations of the presentations are available by request from Dr. Peter Schmidt, MURI Program Manager at ONR. Dr. Schmidt is also fostering stronger collaboration between the two ongoing Navy-sponsored MURI efforts in the area of Railgun Tribology. University of Texas at Austin (PI=Persad) and the Georgia Institute of Technology (PI=Danyluk) lead the two MURI. Dr. Schmidt has hosted several productive joint meetings with both Principal Investigators.

Refereed Journal Articles

1. 1. M. Wang, D. Xu, K. Ravi-Chandar and K.M. Liechti, On the development of a mesoscale friction tester, Experimental Mechanics, 47, (2007), 123-131.

2. 2. D. Xu, K.M. Liechti, and K. Ravi-Chandar, Mesoscale scanning probe tips with sub-nanometer RMS roughness, Review of Scientific Instruments, (in print).

3. 3. D. Xu, K.M. Liechti, and K. Ravi-Chandar, On the modified Tabor parameter for JKR-DMT transition in the presence of a liquid meniscus, Journal of Colloids and Interface Science, (in print).

4. 4. D. Xu, K.M. Liechti, and K. Ravi-Chandar, On the transition from intimate contact to monolayer lubricated contact: Discretized shear strength in frictional sliding, Journal of the Mechanics and Physics of Solids, (in preparation).

5. 5. L. Brown, D.Xu, K. Ravi-Chandar, S. Satapathy, Coefficient of friction measurement in the presence of high current density, IEEE Transactions on Magnetics. 43, (2007), 334-337.

6. 6. S. Satapathy, et. al., "Measurement of friction in railguns using Photonic Doppler Velocimetry." ASME McMat Conference, Austin, TX (2007.)

7. 7. A Study of Magnetic Sawing in an Aluminum Bar D Melton, T Watt, M Crawford - 13th EM Launch Technology Symposium (EML), 2006

8. 8. A Magnetofluid Mechanical Model to Describe Rail–Armature Interface Phenomena V Thiagarajan, KT Hsieh - 13th Electromagnetic Launch Technology Symposium (EML), 2006

9. 9. Eddy Current Effects in the Laminated Containment Structure of Railguns D Landen, S Satapathy - Magnetics, IEEE Transactions on, 2007

10. 10. Railgun Tribology—Chemical Reactions between Contacts C Persad - Magnetics, IEEE Transactions on, 2007 -

11. 11. Railgun Tribology: Characterization and Control of Multishot Wear Debris C Persad , Z. Castro - 13th Electromagnetic Launch Technology Symposium (EML), 2006

12. 12. Results of Copper-Silver Rail Materials Tests Z Castro, C Persad - Magnetics, IEEE Transactions on, 2007

13. 13. Measurement of High-Strain-Rate Adiabatic Strength of Conductors D Landen, S Satapathy, D Surls - Magnetics, IEEE Transactions on, 2007

14. Jin, X., Keer, L. M. and Wang, Q. (2007). A practical method for singular integral equations of the second kind. to appear in Engineering Fracture Mechanics.

15. Electromagnetically Induced Crack Opening Force and Condition for Electric-Breakdown I: General Solutions", by S. Hao, Q. Wang, L. M. Keer; in review

16. Rolling Contact Between Rigid Cylinder and Semi-Infinite Elastic Body with Sliding and Adhesion", by S. Hao and L. M. Keer. J. Tribology, 2007. 129: p. 481-494

17. Chen, W. W., Wang, Q., Liu, Y., Chen, W., Cao, J., Xia, C., Raj Talwar, and Rick Lederich, Analysis and Convenient Formulas for Elasto-Plastic Contacts of Nominally Flat Surfaces: Average Gap, Contact Area Ratio, and Plastically Deformed Volume," to appear in Tribology Letters.

18. 18. Chen, W. W., Wang, Q., Wang, F., Keer, L. M., and Cao, J., "Three-Dimensional Repeated Elasto-Plastic Point Contact, Rolling and Siding," to appear in Journal of Applied Mechanics

19. Chen, W. W., Liu, S.B., and Wang, Q., "FFT-Based Numerical Methods for Elasto-Plastic Contacts of Nominally Flat Surfaces," to appear in Journal of Applied Mechanics.

20. Jin, X., Keer, L.M., and Wang, Q., "A Practical Method for Singular Integral Equations of the Second Kind," to appear in Engineering Fracture Mechanics.

21. Liu, S. and Wang, Q, 2007, "Determination of Young's Modulus and Poisson's Ratio for Coatings," Surface and Coating Technology, Vol. 201, pp. 6470-6477.

22. 22. Martini, A., Velter, G., Keer, L.M., and Wang, Q., 2007, "Maximum Stress Prediction for Rough, Sinusoidal and Textured Surfaces," Tribology Letters, Vol. 27, pp. 61-67.

23. Liu, Y., Chen, W., Liu, S., Zhu, D., and Wang, Q., 2007, "An Elastohydrodynamic Lubrication Model for Coated Surfaces in Point Contacts," Journal of Tribology, Vol. 129, pp. 509-516.

24. 24. Zhu, D., Martini, A., Wang, W., Hu, Y., Lisowsky, B., and Wang, Q., 2007, "Simulation of Sliding Wear in Mixed Lubrication," Journal of Tribology, Vol. 129, pp. 544-552.

25. Martini, A., Escoffier, B., Liu, S., Wang, Q., Keer, L., Zhu, D., and Bujold, M., 2006, "Prediction of Subsurface Stress in Elastic Perfectly Plastic Rough Components," Tribology Letters, Vol. 23, pp. 243-251.

26. Liu, Y., Wang, Q., Hu, Y., Wang, W., and Zhu, D., 2006, "Effects of Differential Schemes and Mesh Density on EHL Film Thickness in Point Contacts," ASME Journal of Tribology, Vol. 128, pp. 641-653.

27. Kim, W.-S. and Wang, Q., "Numerical Computation of Surface Melting at Imperfect Electrical Contact between Rough Surfaces," Proceedings of the 2006 IEEE Holm Conference, pp. 81-88.

28. 28. 1. X. Long, T. Chen, I. Dutta, C. Persad, "Effect of Current Crowding on Microstructural Evolution at Rail-Armature

Contacts in Railguns", IEEE Trans. Magnetics July 2007

29. 29. 2. I. Dutta, C. Park, B. Cleveland, "Electric current induced conformal thin film coatings on micro-patterned structures", manuscript in preparation for Appl. Phys. Lett.

Books and Chapters
None entered

Technical Reports

1. Melton, David Michael. An experimental and computational study of magnetic sawing in a railgun Thesis (M.S. in Engineering)--University of Texas at Austin, 2006.

2. Luc Delaney (lieutenant, U.S Navy), "A FIRST REPORT ON ELECTROMIGRATION STUDIES AT A MODEL COPPER-ALUMINUM RAILGUN CONTACT", M.S. thesis, December 2006.

3. Bryant Cleveland (lieutenant, U.S. Navy), "INTERFACIAL EFFECTS AT ARMATURE-RAIL CONTACTS IN RAILGUNS : Electromigration and Debris formation", M.S. thesis, March 2007.

Contributed Presentations

1. 4. Liu, Y., Wang, Q., Wang, W., Hu, Y., and Zhu, D., 2006, "Experimental Verification of a Mixed Lubrication Model," STLE Annual Meeting, Calgary, Canada.

2. Wang, Q., Nanbu, T, Yasuda, Y., and Zhu, D., "Investigating the Effect of Micro Texture on Lubrication," STLE Annual Meeting, Calgary, Canada.

3. Wang, Q., Nanbu, T, Yasuda, Y., and Zhu, D., "Investigating the Effect of Micro Texture on Lubrication," STLE Annual Meeting, Calgary, Canada.

4. 7. Ghosh, G, Hseih, P., Chung, Y., and Wang, Q., 2006, "Boundary Lubrication Using Liquid Metals," STLE Annual Meeting, Calgary, Canada

5. 8. Quantized friction: the transition from molecular to monolayer lubricated contact", D. Xu, K.M. Liechti and K. Ravi-Chandar, 30th Annual Meeting of the Adhesion Society, Tampa, FL, February 2007.

6. 9. "On the modified tabor parameter for the JKR-DMT transition in the presence of a liquid meniscus", D. Xu, K.M. Liechti and K. Ravi-Chandar, 30th Annual Meeting of the Adhesion Society, Tampa, FL, February 2007.

7. 10. "Scale-dependence friction: the transition from molecular to monolayer lubricated contact", Dewei Xu, Kenneth Liechti, and K. Ravi-Chandar, McMAT 2007, Applied Mechanics and Materials Conference, Austin, TX, June 2007

8. 11. "The modified Tabor parameter for JKR-DMT transition in presence of a liquid meniscus", Dewei Xu, K. Ravi-Chandar, and Kenneth Liechti, McMAT 2007, Applied Mechanics and Materials Conference, Austin, TX, June 2007

Patents

None entered

Honors

1. STLE Fellow
    to: Prof. Q. Wang of Northwestern University
    from: Society of Tribologists and Lubrication Engineers (STLE).
    Election to Fellow Status

2. Editorial board
    to: Prof. Q. Wang of Northwestern University
    from: JOURNAL -Tribology - Materials, Surfaces and Interfaces
    Election to Editorial Board

3. Editorial board
    to: Prof. Q. Wang of Northwestern University
    from: JOURNAL - Advances in Tribology
    Election to Editorial Board

4. Editorial board
    to: Prof. Leon Keer of Northwestern University
    from: JOURNAL - Mechanics of Materials
    Election to Editorial Board

Related Sponsored Work

None entered

The main technical report is structured to show progress on each of the three main tasks. The Tasks are listed in Table 1.Four summaries are highlighted under Task 1 that investigates the physical and chemical interactions and processes that occur at the sliding electrical contact interface. The summaries are: 1.1 Sliding Between Metallic Surfaces, a Numerical Approach; 1.2 Modeling and Understanding the R/A Interface: R/A Contact and Lubrication;1.3: Imperfect Electric Contact Model; 1.4 Mesoscale Electric Contact Probe (MeCOP).Three summaries are highlighted under Task 2 that determines the parameters that control the life of rails in a railgun. The summaries are: 2.1 Modeling and Understanding the R/A Interface: Cracks in EM Fields; 2.2 Application of Photonic Doppler Velocimetry Diagnostics in railguns; 2.3 Railgun Systems Level Bond Graph Model. Two summaries are highlighted under Task 3 that sets out to design, develop, and test functional materials for rail wear control. The summaries are: 3.1 Developing the R/A Interface: R/A Contact and Lubrication: Fusible alloy lubrication of aluminum-aluminum interface; 3.2 Role of Electrical Skin Effects and Current Crowding on the Stability of Armature-Rail Contacts in Railguns.

Table 1: List of Tasks being performed under this ONR MURI Grant

1.0 Investigate the physical and chemical interactions and processes that occur at the sliding electrical contact interface.
➢solid-on-solid sliding electrical contact
➢ liquid-metal-lubricated sliding electrical contact
➢plasma arcing electrical contact

2.0 Determine the parameters that control the life of the rails in a railgun.

➢barrel heating, distortion, and eddy-current effects.
➢wear mechanisms and wear synergisms
➢crack formation and crack growth in fatigue and fracture

3.0 Design, develop, and test functional materials for rail wear control.

➢relate intrinsic materials properties to tribological behaviors
➢effects of lubricants, engineered claddings, control of chemical reactions
➢wear control via lubrication, wear-debris traps, and micro-vibration

1.1 Sliding Between Metallic Surfaces, a Numerical Approach

Investigators
- Prof. Michael Marder, UT Austin, Center for Nonlinear Dynamics
- Evangelos Meintanis, UT Austin, Center for Nonlinear Dynamics

Technical Objectives

To study the effects of high electric current densities in the friction between and resulting wear of metallic surfaces.

Technical Approach

The objective is to be achieved through the numerical modeling of metals at the atomic level. The combination of atomic interaction models with bulk electrodynamic calculations is required to achieve the stated objective.

Progress Statement Summary

In FY2007 we have so far overcome the fundamental hurdles that have frustrated our efforts at combining electrodynamics and molecular dynamics. We have demonstrated our achievements with small scale simulations of atomic systems, under the influence of externally applied electric fields.

Progress

At the end of the previous fiscal year, the computational infrastructure to produce and test the numerical modeling code had been built. That consisted of a four Opteron class processor workstation. On the software front, two components of the code needed to achieve our objective, were individually working. The molecular dynamics code HOLA had been updated to allow use of its MEAM (Modified Embedded Atom Method) derived interatomic potentials with multiple species simulations. This was particularly important to study systems such as the Cu-Al contacts, between the rails and armature in the railgun. Meanwhile, proof-of-concept code for the solution of Maxwell's electrodynamics equations had been produced. The outstanding issue was to merge these components into an efficient single code.

The main issue in merging electrodynamics and molecular dynamics is the disparity of the respective time scales. This difference, of four to five orders of magnitude, is due to the corresponding difference in mass between electrons, the main actors in current flow, and atoms. The problem then is that a full time electrodynamics simulation adds tens of thousands of steps between successive molecular dynamics calculations.
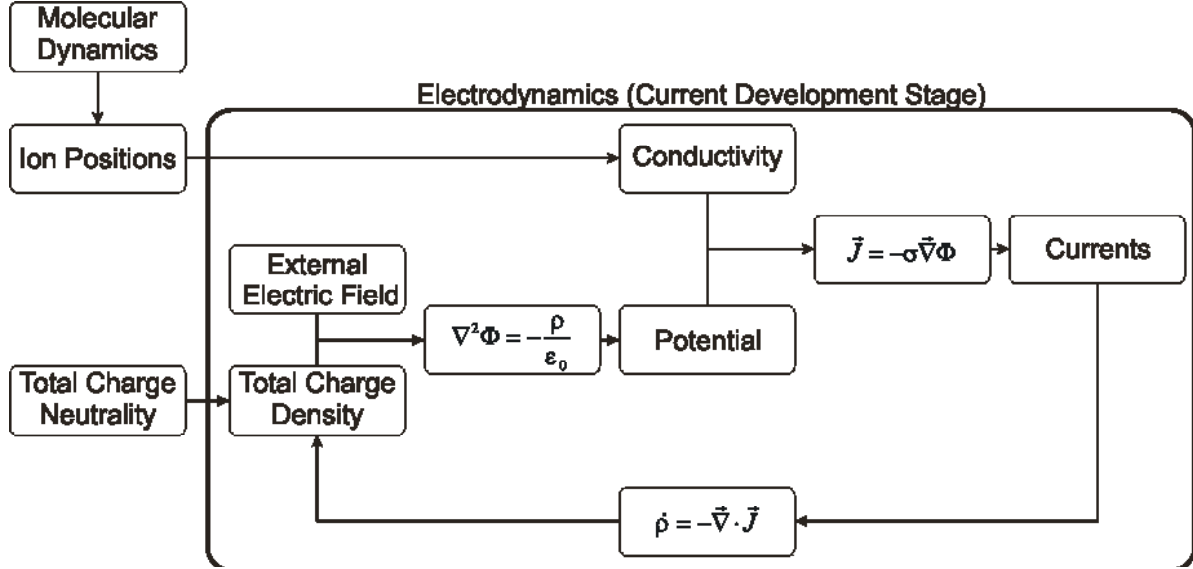
Figure 1

We overcame this problem, by realizing that MD (Molecular Dynamics) as well as the externally imposed boundary conditions set the stage for electrodynamics. The reason for this is that the atom positions determine the conductivity distribution through the simulation volume. During an MD step, this distribution is constant and we expected the electronic charge and current density configurations to reach equilibrium values very fast. This idea governs the way we integrated our electrodynamics solver with the HOLA MD package. Specifically, after each MD step, the solver calculates the conductivity distribution in the computational volume, which in turn allows the iterative application of Poisson and Ohm's law solvers that yield the charge and current density distributions, as well as the electric field, in the system (see). This iterative process is stopped as soon as equilibrium has been reached. The current density and electric field information *Figure 2*
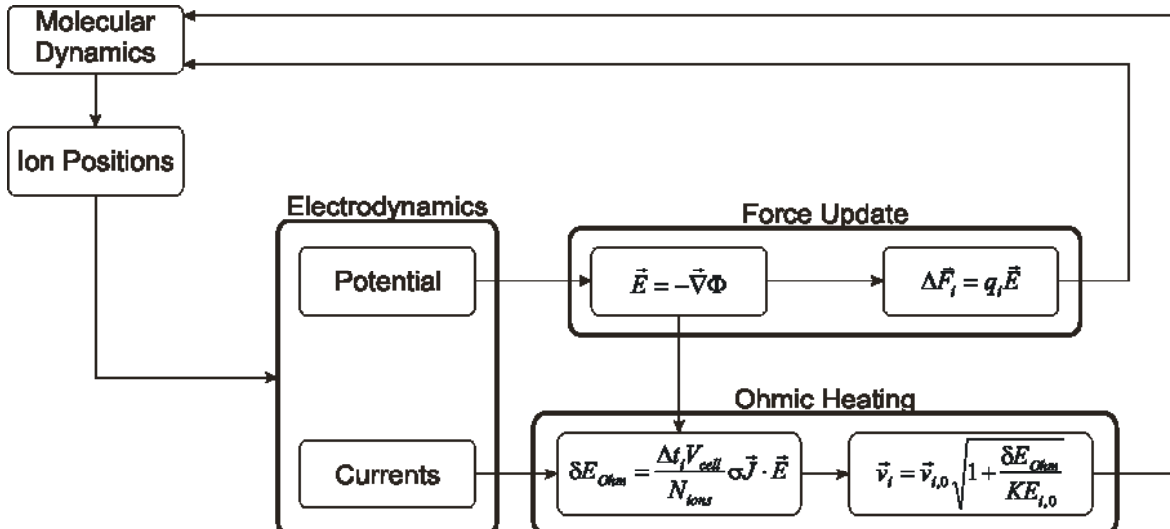
is fed back into the MD simulation, in the form of direct forces on the atoms and heating of the material (see). This is achieved because the atoms are considered ionized for the purposes of these calculations. The latter is accounted for by random "kicking" of the relevant atoms. It should be noted that magnetic fields are currently neglected. This issue will be addressed in the future and the code is structured to facilitate their addition.

For the performance of basic sanity checks and to aid the qualitative interpretation of our data we have developed visualization, post-processing software. This was done within Matlab and it allows us to examine both snapshots (see) and movies of the evolving systems.

Our demonstration runs have validated our approach. Electrodynamic convergence is typically achieved after a few hundred iterations of the relevant subroutines. Our tests with small systems reproduce the expected physical behavior. We are therefore confident of the efficiency of our computational approach and its scalability to larger systems.

Specifically, we have started with tests of single material wires (such as the one in) that we could make explode at the right electric current values, in the expected time-frame. We are now conducting tests with a small tip of one material pressed on a flat block of another, while an external electric field is applied. The materials are Cu and Al. This kind of setup is typical of laboratory friction measurement experiments. To be able to drag the tip along the face of the block, a system of virtual springs has been implemented to keep the tip upright and the normal force between the two bodies constant. Another set of virtual springs applies measurable, horizontal force to the tip. Knowledge of the forces allows us to measure the static and dynamic coefficients of friction in the system. Movies from these simulations are available online[1,2].

Concurrently, we are working towards parallelizing the newest additions to the code, to allow large scale runs on the supercomputing resources available. Such runs should allow direct comparisons to experimental data and the verification of our simulations.

Figure 3

---
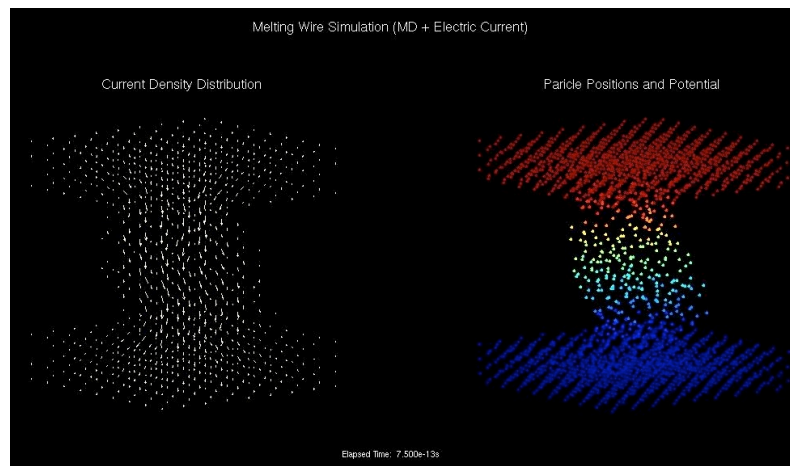
[1]   http://chaos.utexas.edu/~meinv/documents/Shrt_cap_ed_mov-2.wmv

[2]   http://chaos.utexas.edu/~meinv/documents/Styl_blck_30mps_sl_mov-correct_aspect.wmv

4

1.2 Modeling and Understanding the R/A Interface: R/A Contact and Lubrication

Personnel

Qian Wang, L. M. Keer, Y.W. Chung, H. S. Cheng, Professors
Y. Lu, Post Doctoral Fellow
W. Chen and N. Ren, Graduate Students

Technical Objectives

(1) Simulating the contact and lubrication process from contact initiation to motion for deep understanding of interfacial physical phenomena.
(2) Providing an effective and efficient approach/tool for surface/interface virtual design.

Technical Approach

For mixed lubrication, where the contact area and lubrication area are coexisted, the temperatures in the contact area are calculated by solving the boundary condition of equivalent temperatures on the two surfaces with an unknown hear partition coefficient; the temperatures in the lubrication area are obtained by solving the energy equation with moving surface boundaries.

Progress Statement Summary

In 2007, we have studied the effect of coating on isothermal EHL in 3-D line contacts. Due to the use of Continuous Convolution and Fast Fourier Transformation (CC-FFT), the model for 3-D in point contacts was enable to handle the periodic roughness for 3-D line contact model. The coating effect on lubrication was investigated by coupling the elastic deformation of coated surfaces into the lubrication model. It is found that thick thermal softening metals (just like a complaint coating) can improve the film thickness by introducing even larger compliance of surfaces in the application of melting lubrication under the elastic isoviscous EHL condition. This behavior can be used as a possible approach to reduce friction and wear in mixed lubrication. We also started to build up the thermal mixed EHL model in 3-D line contact as reported in this report.

Progress

Figure 1 describes the interaction of surfaces and possible problems involved. Understanding and modeling the initial contact is the first step leading to the investigation of the physical and chemical interactions and processes at the rail-armature contact interface. The contact-to-melt process is the major attention of the research at the current stage. However, the interface is over a large contact region, and materials in the

5

interface undergo elastic and plastic deformations and melting (armature). Proper surface design will help enhance metal lubrication. Figure 2 shows a systematic modeling sequence for the interface from contact to metal lubrication.
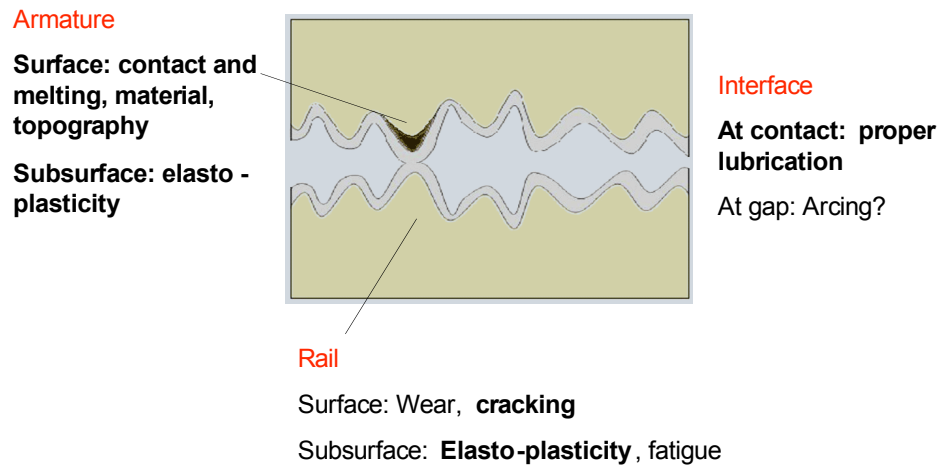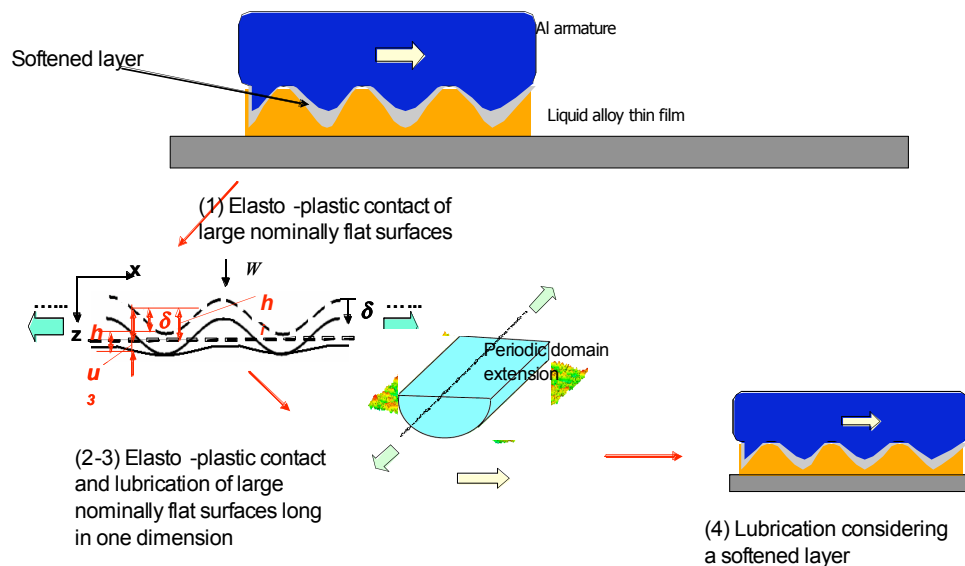
Armature

Surface: contact and melting, material, topography

Subsurface: elasto - plasticity

Interface

At contact: proper lubrication

At gap: Arcing?

Rail

Surface: Wear, **cracking**

Subsurface: **Elasto-plasticity**, fatigue

Figure 1 A rail/armature interface

Al armature

Softened layer

Liquid alloy thin film

(1) Elasto -plastic contact of large nominally flat surfaces

Periodic domain extension

(2-3) Elasto -plastic contact and lubrication of large nominally flat surfaces long in one dimension

(4) Lubrication considering a softened layer

Figure 2 Interface modeling system

(1) Very large rough surfaces in contact

The interaction between a rail and an armature involves very large surfaces, which lead to a large apparent contact area. A change in the distribution of asperity heights and the

6

properties of materials may have a significant effect on the contact behaviors of rough surfaces. A three-dimensional numerical elasto-plastic model for the contact of nominally flat surfaces has been developed based on the periodic expandability of surface topography (Figure 3). This model is built on two algorithms: the continuous convolution and Fourier transform (CC-FT) and discrete convolution and fast Fourier transform (DC-FFT), modified with duplicated padding. This model considers the effect of asperity interactions and gives detailed description of subsurface stress and strain fields caused by the contact of elasto-plastic solids with rough surfaces. Formulas of the frequency response functions (FRF) for elastic/plastic stresses and residual displacement are given in this paper. The model is verified by comparing the numerical results with several analytical solutions. A comprehensive investigation of the effects of topographical parameters and material properties has been conducted (Figure 4), which is a critical step towards understanding friction, wear, lubrication and electrical contact resistance in tribological systems. This model system has resulted in a three-dimensional line-contact model.
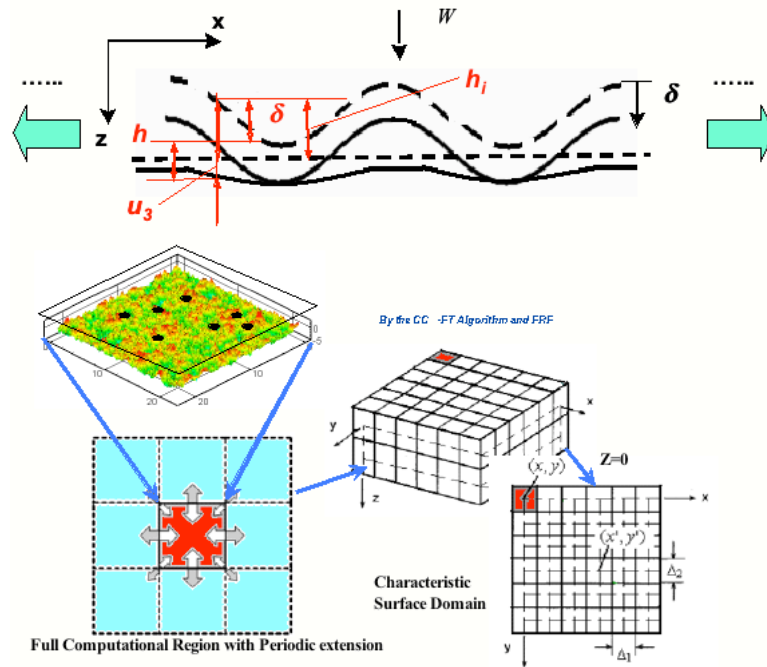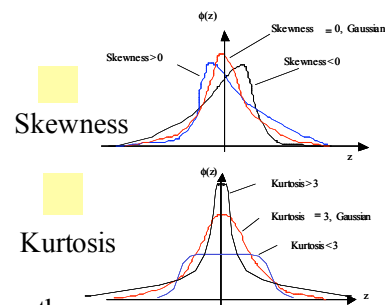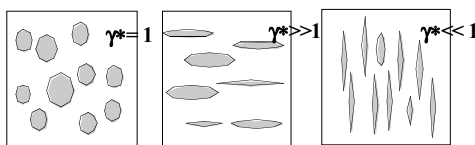

Figure 3   Periodic extension for the modeling of large surfaces in contact

Input:

$$\Sigma = V_p / A_n R_q$$
$$\chi = \beta_y / \beta_x \cdot R_q^A \quad (\beta_y \geq \beta_x)$$
$$\Gamma = h / R_q$$

Ratio of correlation length

$\gamma* = 1$ $\gamma* \gg 1$ $\gamma* \ll 1$

Skewness

Kurtosis

Ratio of equivalent Modulus over yield strength

Hardening modulus ratio   Dimensionless average pressure
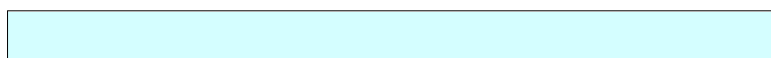
Investigated contact performances

Dimensionless average surface gap $L = \bar{p} / Y$
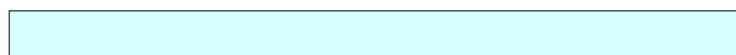
Contact area ratio
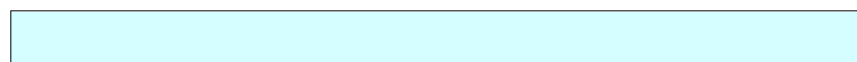
Dimensionless volume with plasticity

Average gap:

Contact area ratio:

$$\Omega = 0.009524 \cdot 10^{s*(\theta - 0.02315 \cdot)} \cdot (\gamma * \chi)^{p1} \cdot (s k \cdot (s k) + 1)^{(\lambda - 0.08169)} K^{(\theta - 0.04049)} M^{p5} M_s^{m5} L^{p12}$$

Plasticity volume:

| Interface status | Material deformation | Fatigue-life analysis |

Figure 4   Effects of topographical parameters and material properties

(2) Line-contact lubrication

The armature motion start from a line contact; and moreover, line-contact elastohydrodynamic lubrication (EHL) is one of the most common types of lubrication of machine components. It is found at the interfaces between gear teeth and cam and follower, and in roller bearings. These components often operate under the mixed EHL conditions where a part of the applied load is supported by surface asperity contact. Surface roughness plays a crucial role in the mixed lubrication of tribological components.

In a typical line contact, the contact interaction area can be infinitely long, by definition, along the length direction. Such a geometric feature favors the modeling of line-contact problems with the well-known plain-strain approach. The two-dimensional (2D) Reynolds equation and contact mechanics form the theoretical basis for line-contact EHL solutions of smooth surface problems. However, the consideration of surface roughness invalidates the use of 2D theories because micro asperity contact and flows around asperities are three-dimensional (3D). A three-dimensional line-contact mixed-elastohydrodynamic lubrication model (3D L-EHL) has been developed based on the line-contact model developed in the research described in the section above for solving rough-surface lubrication problems involving line contacts.

In order to validate this model, an unlubricated line contact is analyzed with the current contact model and a 2D contact analysis. A smooth-surface EHL solution obtained from the current model is compared with that from a conventional 2D EHL model. Good agreements are observed. The following figures show two examples, a line contact involving an isotropic sinusoidal rough surface and a line contact involving a transverse sinusoidal rough surface.
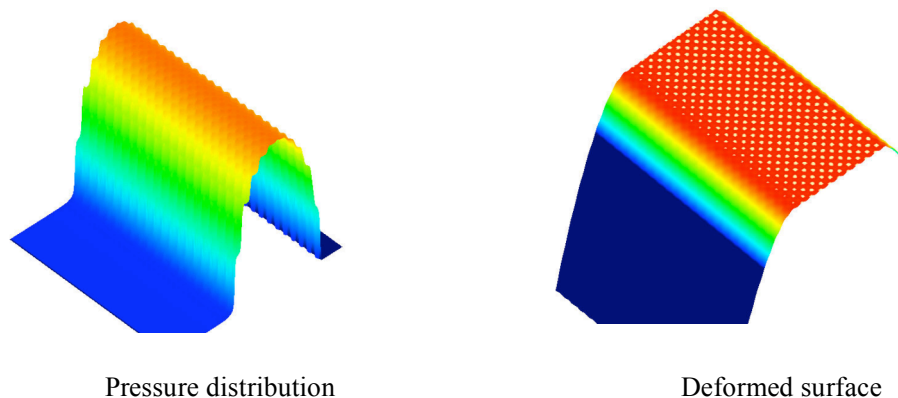

Pressure distribution   Deformed surface

Figure 5 Mixed-EHL solution for a line-contact problem involving an isotropic sinusoidal surface.

9

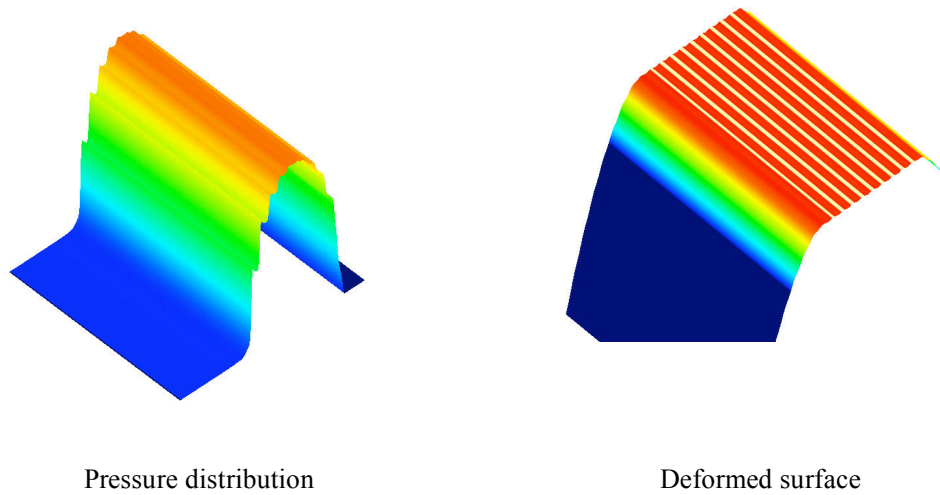| Pressure distribution | Deformed surface |

Figure 6   Mixed-EHL solution for a line-contact problem involving a transverse sinusoidal surface.

Figure 7 summarizes the average film thickness as affected by roughness orientations using generated sinusoidal surface. The results indicate the preference of transverse surfaces in such line contacts for lubrication enhancement.
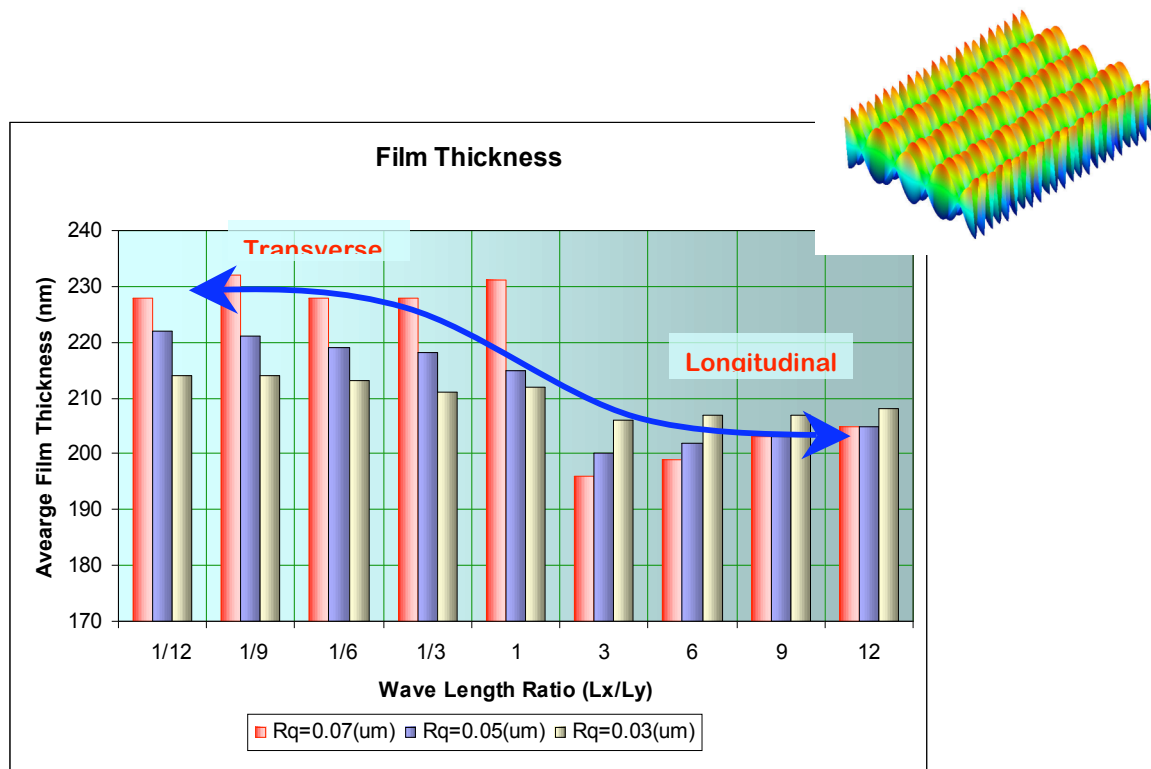
Figure 7 Effect of surface roughness orientation on film thickness

(3)   Three dimensional line-contact lubrication involving a softened layer

The surface material softened due to heating may be treated as a soft coating. Elastohydrodynamic lubrication (EHL) models for coated surfaces for line and loint contacts have been developed by combining the elastic deformation formulation for the coated surfaces with an EHL model. Inverse fast Fourier transform (IFFT) is employed first to obtain the influence coefficients (ICs) from the frequency response function (FRF). In order to reduce the aliasing effect in the frequency domain, the domain is extended. The subsequent calculation of elastic deformation is performed using the efficient algorithm of discrete convolution and fast Fourier transform (DC-FFT). The coating EHL model is verified by the comparison to available numerical results. The effects of coating on lubrication under various loads, speeds, rheological models and pressure-viscosity behaviors are numerically investigated. Similar to the observations from dry contact, soft coatings in EHL tend to increase the nominal contact radius but reduce the maximum contact pressure, and vice versa for more stiff coatings. However, as coating thickness increases, the influence of coatings on film thickness, including the central and the minimum film thicknesses, does not follow a monotonic variation, and therefore, can not be predicted by any simple film thickness equation. The reason for that is pressure viscosity effect which tends to counterbalance the effect of coating. The average friction coefficient in lubricant film increases in hard coating cases but decreases for soft coating cases. Furthermore, two possible approaches to improving the minimum film thickness thus reducing friction and wear in mixed lubrication are indicated: a thin stiff coating for conventional EHL and a thick compliant coating for soft EHL. These analyses suggest that surface softening does not decrease the strength of melting lubrication (Figure 8).
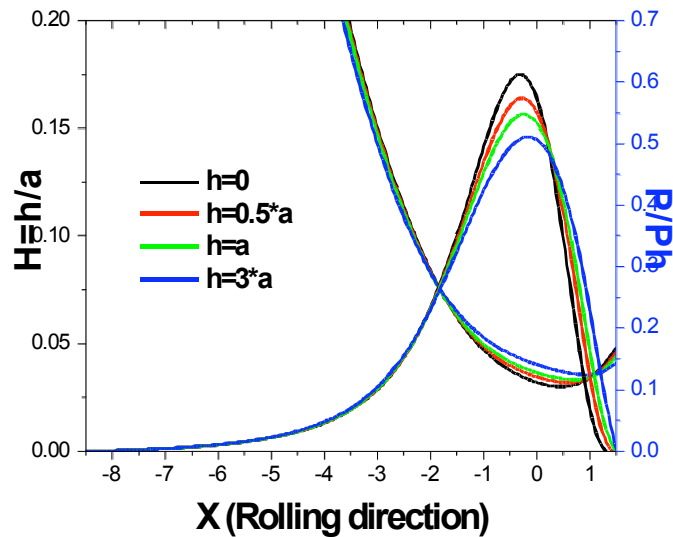

Figure 8   Effect of a soft layer on melting lubrication: increased film

thickness and decrease pressure peaks.

(4)   Metal lubrication in a thermal environment

Temperature plays an important role in the process of friction. A comprehensive thermal model will provide a basis for analysis of possible sliding failure. Energy equation controls the temperature in lubricant. To obtain the precise temperature distribution of lubricant, a natural choice is to solve the energy equation directly. However, difficulties rise when the approach is applied to the mixed lubrication, the costly discretization in the direction normal to the film thickness, and the discontinuity at the position of asperity contacts. In this study, the 3-D temperature distribution in mixed EHL is calculated by simultaneously solving the energy equation for lubrication area and temperature continuity condition for contact area.

As shown below, the Carstesian coordinate axes are fixed at the center of a computation domain. Two surfaces in contact move along the direction of x with velocities u_1 and u_2. Suppose an instantaneous point heat source of strength $q(x',y',t')$ in the contact area emitted at position (x', y') and time t' with no heat loss on the boundary. The heat fluxes assigned to two surfaces in dimensionless form are
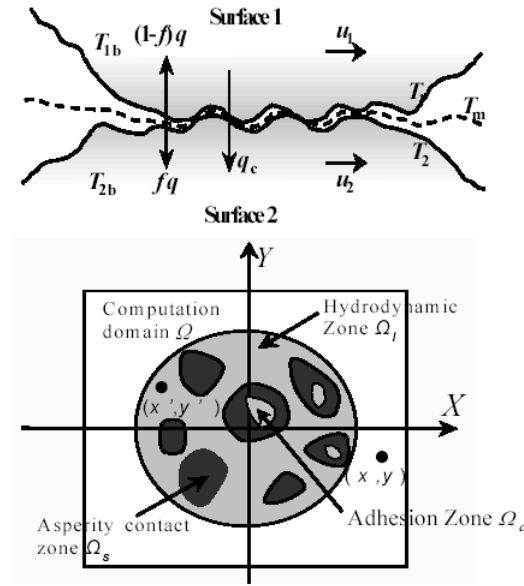

Figure 8   Physical model of thermal analysis for mixed lubrication in point contacts

$$\begin{cases} \overline{q}_1(\overline{x}',\overline{y}',\overline{t}') = [1 - f(\overline{x}',\overline{y}',\overline{t}')]\overline{q}(\overline{x}',\overline{y}',\overline{t}') \\ \overline{q}_2(\overline{x}',\overline{y}',\overline{t}') = f(\overline{x}',\overline{y}',\overline{t}')\overline{q}(\overline{x}',\overline{y}',\overline{t}') \end{cases}$$

(1)

where $f(x',y',t')$ denotes a partition coefficient. The temperature rises on two surfaces at

position (x,y) from time 0 to t can be thus expressed in dimensionless form as

$$\Delta \overline{T}_i(\overline{x},\overline{y},\overline{t}) = \int_0^{\overline{t}} \iint_\Omega \frac{\overline{q}_i(\overline{x}',\overline{y}',\overline{t}')\,\mathrm{d}\overline{x}'\,\mathrm{d}\overline{y}'\,\mathrm{d}\overline{t}'}{(\overline{t}-\overline{t}')^{3/2}}$$
$$\times \exp\left\{-\frac{[(\overline{x}-\overline{x}')-\overline{u}_i(\overline{t}-\overline{t}')]^2+(\overline{y}'-\overline{y})^2}{(\overline{t}-\overline{t}')}\right\} \qquad (i=1,2)$$

(2)

The heat flux intensity caused by friction can be expressed approximately as

$$\overline{q} = \mu \overline{p}\left|\overline{u}_1 - \overline{u}_2\right|$$

(3)

where μ is the friction coefficient for asperity contact area.

The boundary condition is temperature continuity as follows

$$[\overline{T}_{2b} + \Delta \overline{T}_2] - [\overline{T}_{1b} + \Delta \overline{T}_1] = 0$$

(4)

The equation is used to determine the heat partition coefficients.

Eqs. (1) and (2) are two convolution equations whose discrete solutions can be obtained through FFT-based fast algorithm. In general the calculation includes two steps, determination of influence coefficients and multi multiplication and summation. According to different schemes of approximation influence coefficients with different precisions are obtained. Multi multiplication and summation can also be performed by Multi Level Multi Integration (MLMI), but the FFT-based algorithm has higher efficiency. However, different from the calculation of elastic deformation, the influence coefficients here have to be reversed in order before the influence coefficient matrix is transformed into the frequency domain by applying FFT algorithm.

For hydrodynamic lubrication the energy equation for Newtonian fluid is

$$\rho_f c_f\left(u\frac{\partial T}{\partial x} + v\frac{\partial T}{\partial y}\right) = k_f \frac{\partial^2 T}{\partial z^2} + \beta T\left(u\frac{\partial p}{\partial x} + v\frac{\partial p}{\partial y}\right) + \eta\left[\left(\frac{\partial u}{\partial z}\right)^2 + \left(\frac{\partial v}{\partial z}\right)^2\right]$$

(5)

The left term of the equation is the convection term related to the lubricant flow while the right terms represent in turn the heat conduction, compression work caused by the pressure gradient, and shear heat caused by viscous shear stress.

The flow rate equations are

14

$$\begin{cases} u = \dfrac{1}{2\eta}\dfrac{\partial p}{\partial x}z(z-h) + (u_2 - u_1)\dfrac{z}{h} + u_1 \\[3mm] v = \dfrac{1}{2\eta}\dfrac{\partial p}{\partial y}z(z-h) \end{cases}$$

(6)

The change of viscosity and density of lubricant are based on free-volume model.

If heat partition is given as a constant for the contact area, the calculation of heat fluxes requires the knowledge of temperature while the temperature itself has to be obtained from the heat fluxes. Numerical iterations are required to determine the primary heat fluxes. Secondly, if heat fluxes are invariable, heat partition can be calculated from an iterative loop that is the same as in the original model. However, the difference is that in present scheme a change in heat partitions will cause consequent changes in the temperature distribution and heat fluxes. For this reason, a cascade iteration loop is employed in this study, as illustrated in Fig. 9. The first iterative loop is designed to get heat fluxes and temperature. After heat fluxes are determined primarily, heat partition has to be checked. If the precision criterion is satisfied, the iteration stops. Otherwise the computation goes to the second iterative loop for correcting the heat partition. Once heat partitions satisfy the demanded precision, heat fluxes have to be checked too. The computation cycle goes on in this way until both heat fluxes and heat partition satisfy the precision criterion.

The 3-D temperature distribution for lubrication area is obtained using the finite differential method (FDM). Along the film thickness, the energy equation was solved at 21 equidistant nodes. From the lubrication area with the 3D mesh to the contact area with 2D mesh, the dummy nodes are used to link these two.
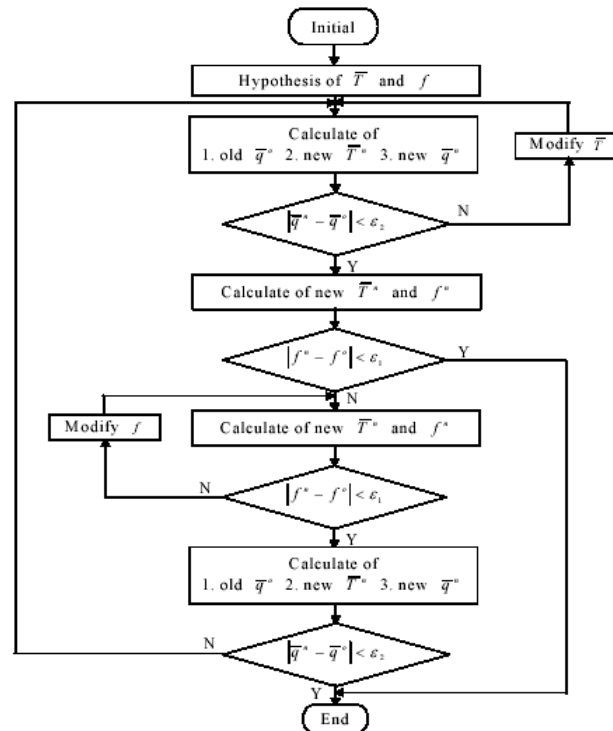
Initial

Hypothesis of $\bar{T}$ and f

Calculate of
1. old $\bar{q}^o$ 2. new $\bar{T}^n$ 3. new $\bar{q}^n$

Modify $\bar{T}$

$\left|\bar{q}^n - \bar{q}^o\right| < \varepsilon_2$ N

Y

Calculate of new $\bar{T}^a$ and f^a

$\left|f^a - f^o\right| < \varepsilon_1$ Y

N

Modify f

Calculate of new $\bar{T}^a$ and f^a

$\left|f^a - f^o\right| < \varepsilon_1$ N

Y

Calculate of
1. old $\bar{q}^o$ 2. new $\bar{T}^n$ 3. new $\bar{q}^n$

$\left|\bar{q}^n - \bar{q}^o\right| < \varepsilon_2$ N

Y

End

Fig. 9   Flowchart of iterations of heat flux and partition in the first correction

In conclusion, the thermal model for mixed lubrication and numerical method for that was developed. The model integrated different models for lubrication area and contact area respectively. The model needs to finalized by code development and validated through the comparison with available experimental measures.

1.3: **Imperfect Electric Contact Model**

Investigators: Dr. Sikhanda Satapathy (512) 232-4455, sikhanda@iat.utexas.edu and Prof. Laxminarayan L. Raja

Technical objective: Develop a Imperfect Electric Contact Model for sliding contact under current transfer conditions prevalent in the armature-rail interface of the railgun.

Technical approach:

Numerical techniques appropriate for modeling arcing contact are being developed to study armature-rail interface contact. These techniques will be used to study current division between solid-solid and arcing contact before and after armature transition.
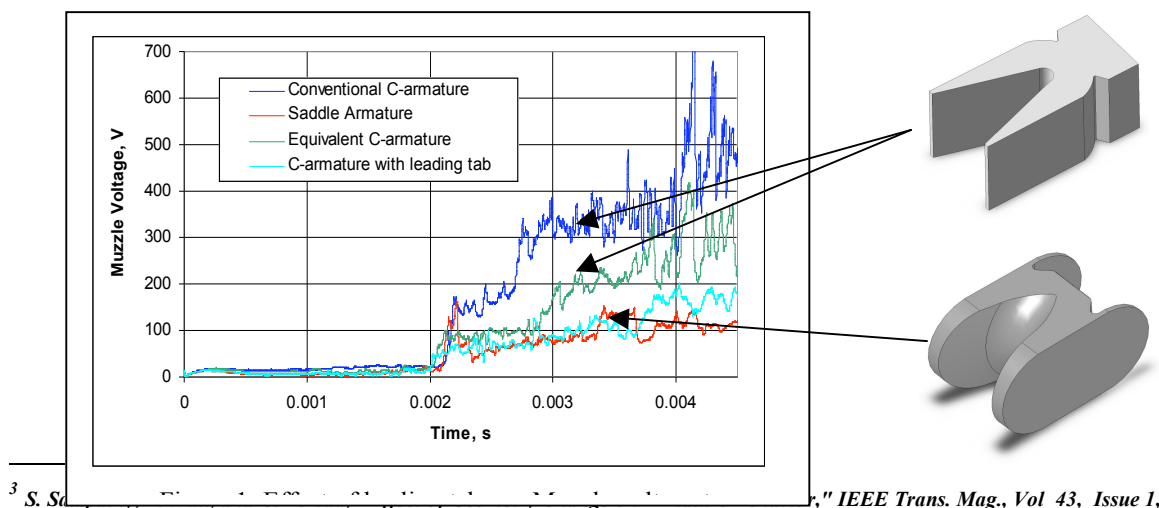
Progress statement summary:

A mixed contact regime has been identified from experimental data, which indicates that solid-solid and arcing contact may coexist. Computational technique development is underway for modeling of the microdischarge plasma in asperity level voids and larger scale diffuse plasma under conditions of significant gap separation.

Progress:

The armature-rail (AR) interface not only presents challenges in measurement of operating conditions, it poses a complex multi-physics environment for modelers as well. The asperities at which the contact is made, undergo melting and vaporization along with plastic deformation in the solid phase.

Comparison of test results[3] for C-armatures and saddle armatures showed that not only was the running voltage lower for the saddle armatures, the post transition voltage was also found to be much

Figure 1. Effect of leading tab on Muzzle voltage transients

[3] S. Satapathy, Figure 1. Effect of leading tab on Muzzle voltage transients," *IEEE Trans. Mag., Vol 43, Issue 1, Part 2, Page(s) 408-412, 2007*

lower for the latter. These results indicate that the tabs in saddle armatures are in good contact with the rail, while arcing but occurs in the trailing arm area after transition. Then the question arises, how much current is divided between the arcing and the solid contact? The answer to this question is critical to designing an armature, which might be more resistant to post transition effects. In other words, if the current in the arcing area can be minimized by providing alternate current paths, rail damage can be significantly reduced.

We are developing a detailed first principles model of plasma phenomena occurring in contact gaps during motion of a metal armature through a railgun. The plasma discharge in the contact gap is expected to be a high-pressure, weakly non-ideal plasma. The plasma discharge potentially provides a major mechanism for electrical conductivity through the contact gap. The plasma is also a major source of thermal dissipation in the system and importantly causes rail erosion, impacting the overall lifetime of the system. Understanding the nature of these contact plasmas is therefore of critical interest. The model will also provide a detailed description of the thermal energy dissipated in the large gap regime owing to plasma activity.

18

1.4 Mesoscale Electric Contact Probe (MeCOP)

Investigators

K. Ravi-Chandar

*Technical   **Objectives**   *****

The main objectives of this research is to build a mesoscale friction tester (MFT) and to augment it with an electrical current capability. With this apparatus, we will examine the influence of current transport on the friction and wear characteristics of the contact pair. The scale of contact is expected to span from about 10 nm to about 10 μm.

*Technical   **Approach***

The technical approach is based on fundamental experimental investigations; with the aid of the mesoscale apparatus, we probe the friction and wear characteristics of interfaces that transport current. With this in mind, we bring two metallic surfaces together, with a controlled interfacial roughness, measured normal force and a known frictional sliding. The experimental measurements are intended to provide mechanisms for modeling frictional contact.

*Progress   **Statement**   **Summary***

The design, fabrication and calibration of the MFT were completed in the previous year of the program; they are documented in a recently published paper [1]. Smooth probes with an RMS roughness of about 0.2 nm and a radius in the range of 500 nm to 50 μm have been fabricated from tungsten wires, by modifying an electrochemical etching process [2]. Such probes are essential in the study of single asperity contact problems. Interpretation of the friction experiments requires an appropriate contact mechanics model in order to identify the area over which frictional sliding occurs; selection of appropriate contact models in the presence of a surface layer of moisture was examined and reported [3]. Friction measurements on scales ranging from 10 nm to 1 μm have been performed in examining contact between two idealized surfaces – a smooth tungsten probe and a nearly atomically flat mica sheet. These experiments have provided key insight into a scale dependent discrete transition in friction from intimate atomic contact between the sliding pairs to a lubricant mediated sliding; (adsorbed water or hydrocarbons act as the lubricating medium) [4]. Initial experiments on the influence of current passage through the contact have been completed [5]; these experiments demonstrate the capability of the instrument and also reveal that frictional resistance increases markedly with electrical transport.

Progress

We have completed all preliminary experiments that are aimed at calibrating the apparatus, establishing the contact mechanics models necessary for interpretation of the experimental data, and frictional studies that bridge scales from micro down to nano scales in contact between tungsten and mica. With this effort, documented in three publications, we are confident that the instrument is functioning at the resolution that is required. Furthermore, this study has revealed some fundamental

aspects of friction under single asperity contact. This enables an examination of the influence of electrical transport across the contact region on friction and wear characteristics. Figure 1 shows the forces measured in a friction experiment with a tungsten probe on a copper surface. Initially, the normal force is increased to a level of about 0.3 V; then, the sliding actuator is energized and a scan is initiated. The friction force builds up to about 0.2 V and sliding begins at this level, with a constant normal force. At about 20 μm into the scan, the electrical current is turned on; immediately, there appears to be an apparent increase in the normal force, which is in fact triggered the blow-off force generated as soon as the electrical current is turned on. A study of the blow-off force has been conducted and the results are currently being examined. Furthermore, the frictional sliding exhibits a stick-slip response, with significantly increased frictional resistance. The stick-slip wavelength appears to correlate well with the grain size distribution suggesting that there appears to be a microstructural influence on current transport effects. This requires further study. Scanning electron micrographs of the scan track (after 100 repeated scans over the same line) are shown in Figure 2; at low magnification, the wear groove is visible. EDS analysis of the composition in this region indicates that tungsten from the probe has been deposited on the wear scar. Furthermore, the nearly circular scars visible in the high magnification image in Figure 2 indicate that arcing has occurred in the contact region (the current densities are in the range of 10^9 A/m^2).
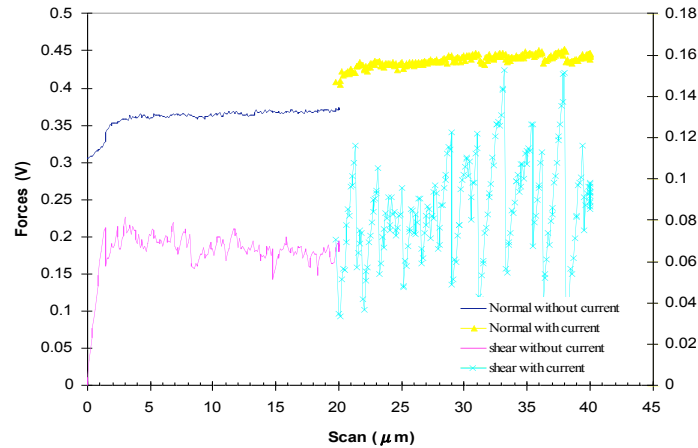

Figure 1. Variation of normal and sliding force with scan distance; sliding after a scan distance of 20 μm occurs with electric current transport across the contact area.
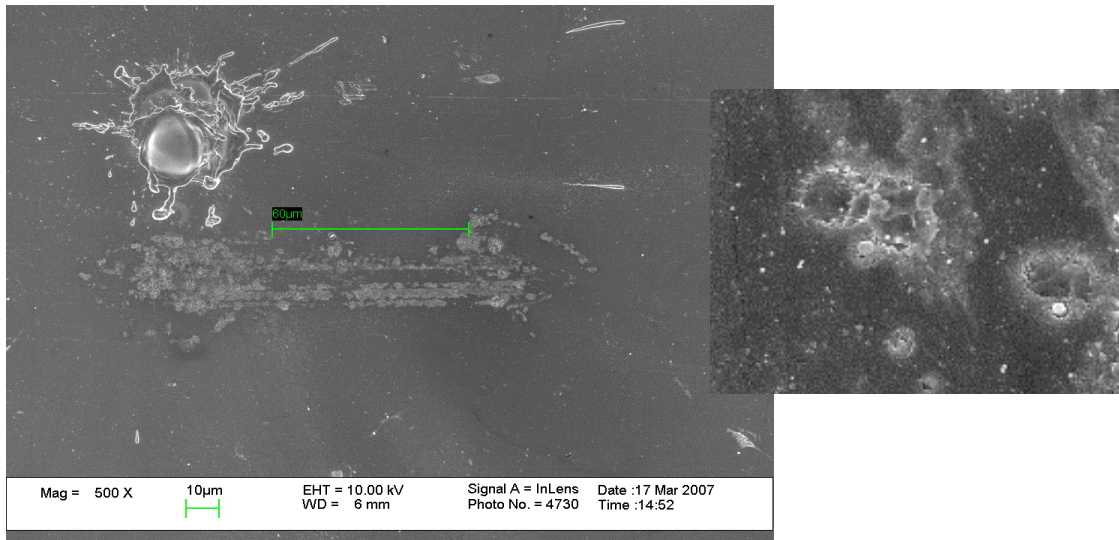
20

Figure 2. (a) Wear scar of a tungsten probe scratching on a copper specimen, with electrical transport across the contact region. Transfer of tungsten to the copper was observed by EDS. (b) The circular spots observed in the high magnification image are considered to be evidence of arcing across the contact region.

2.1 Modeling and Understanding the R/A Interface: Cracks in EM Fields

Personnel

Leon M. Keer, Professor, Mechanical and Civil Engineering

Qian Wang, Professor, Mechanical Engineering

Su Hao, Post Doctoral Fellow, Mechanical Engineering

Xiaoqing Jin, Post Doctoral Fellow, Mechanical Engineering

Technical Objectives

Experiments on pre-notched conductive plates [Satapathy, 2005], have illustrated that the distribution of the electric current density can be highly concentrated near the crack-like defects. Investigating this destructive phenomenon is beneficial to the development of practical applications of the railgun technology, so as to provide useful information for rail design with enhanced performance in fracture and wear resistance.

The singular electric field will lead to a highly disturbed magnetic field near the crack, resulting in an unevenly distributed Lorentz force. Evaluation of the coupling electro-magneto-mechanical effect calls for a reliable computational scheme for the magnetic field. A two-dimensional (2D) model of the magnetic field is proposed by introducing some plane strain type assumptions in linear elasticity theory. To validate these simplifications through a comparative study, a 3D computation is performed in this study.

Technical Approach

The magnetic field in a conductive plate containing an elliptical hole is analyzed in both 2D and 3D computational models. The 2D study uses the potential theory which reduces the static electro-magnetic (EM) field to a governing Laplace equation. In representation of the elliptic coordinates, the closed-form solution is derived by the method of separation of variables. In the 3D analysis, a semi-analytical method (SEM) is employed in the computation. The elementary solution of a rectangular conductor is derived analytically. The computationally domain is discretized into rectangular meshes. The resultant field distribution is evaluated numerically by superposing the contribution from each element.

Progress Statement Summary

1. Introduction and Planed Tasks:

Fatigue life of railgun accelerator (rail track) is a crucial issue among many others for the

development of high-performance electromagnetic launch system. This is because each launching represents a load cycle to the track; this load is a combination of the pressure caused by mechanical contact, stresses and forces induced by applied electromagnetic fields, and the thermal shock resulted by friction, electrical resistance-induced thermal dissipation and arcing (electric-breakdown) between contact surfaces. Therefore, the endurance of a launch machine is essentially determined by the process of low-cycle fatigue-induced material failure at the weakest link of the system: the track surface. The corresponding fatigue life is determined by the mutual functions and interactions of the basic material properties such as strength, toughness, density, magnetic permeability, electrical and thermal conductivities.

Based on the previous work[1-7], the researches to be reported can be described as a sub-program of Northwestern University term to the Navy Railgun project, which includes the following four steps:

(i)   Establishment of a multi-scale, multi-physics model based on the electrical and mechanical analogies between crack problems and armature/track contact;

(ii) Theoretical and numerical analysis to identify the dominant mechanisms that causes material's failure and to find the conditions and criterion for the failure;

(iii) Collaborating with experimental research to explore issues in engineering applications and to verify obtained theoretical solutions;

(iv) Providing analysis-based, engineering-applicable quantitative information and recommendations to assist experimental study and design of launching system with better performance.

As an annual report for the on going project, the works carried out in the past year were focused on (i) and (ii) [8]. The details of the obtained results and conclusions will be given in the following sections. However, the effort on (iii) has already been committed . Toward to build up a solid foundation for the objectives required by (iv), the results obtained so far from (i),(ii),(iii) and the associated methodology developed seem promising. A brief description about this perspective will also be given in this report.
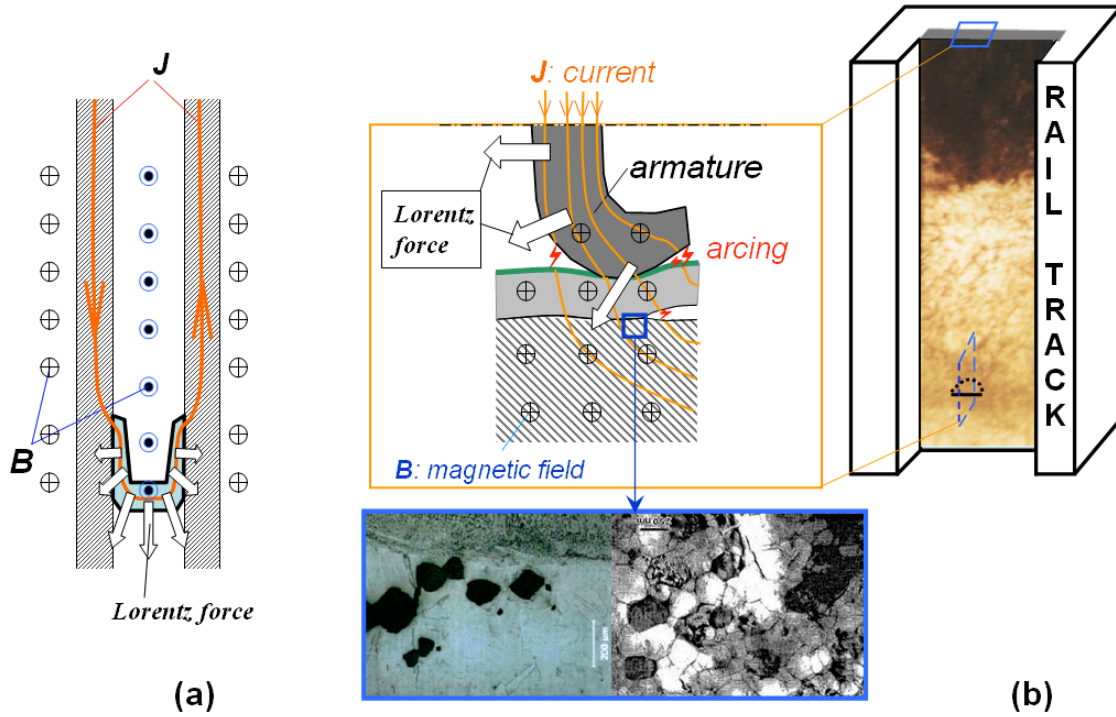
Fig. 1 (a) The launching system of railgun; (b) The weakest link: the rail track contact surface

2 A Multi-Physics Crack Model with Duel Roles

As illustrated in Fig. 1, the armature/rail track contact can be considered as a heterogeneous material system with various discontinuities. When electrical current presents, the associated magnetic field produces Lorentz force that pushes armature moving forwards with additional pressure towards rail track. The discontinuities, such as the contact surface between armature and track or the interface surfaces between different material phases, create higher stresses and electrical current density than that in uniform phase. At the edges of these discontinuities, these additional stresses and current density reach their peak values, which are the driving forces to trigger the nucleation of damages in the forms of voids or micro-cracking and to induce the subsequent macrocrack formation and growth. On other hand, the localized high electrical current density is accompanied with high voltage gradient along the curved discontinuous surfaces; the product of current density and voltage gradient is proportional to the density of energy dissipation. This localized high energy dissipation may result in either electric-breakdown or localized high temperature and subsequent material's melting. Both the cases will cause permanent detriment of the track material by reduction of the capacity against crack growth. Therefore, the primary task of this research is to establish an analytical model to cover involved phenomena at multiple scales while to identify the dominant mechanisms that governs the underlying physical process.

24
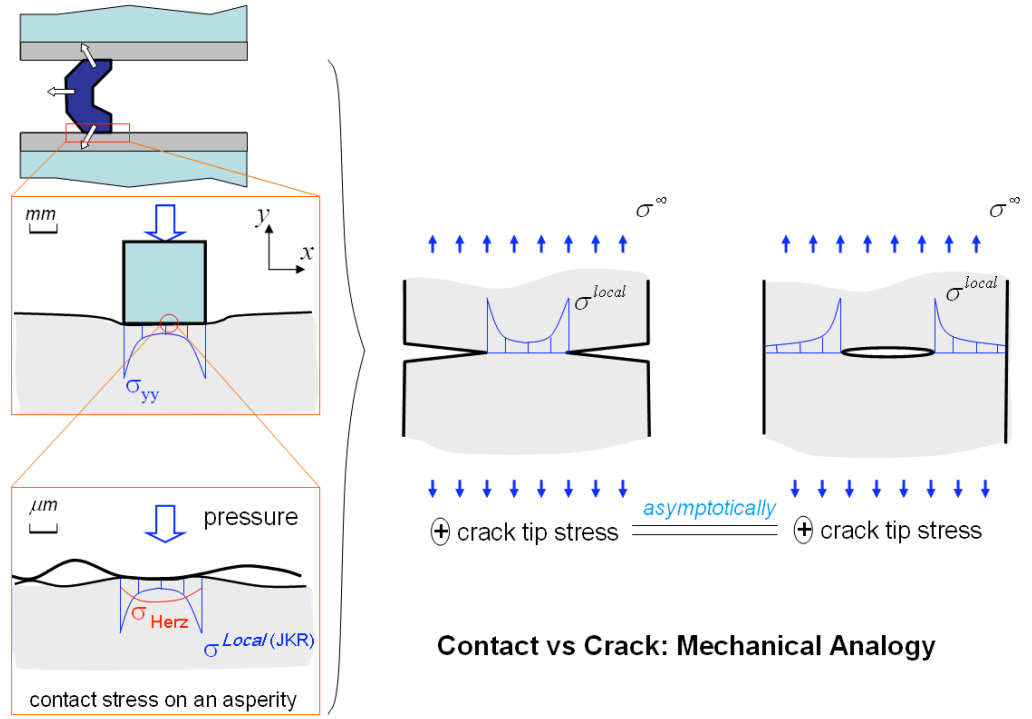
Contact vs Crack: Mechanical Analogy

(a)
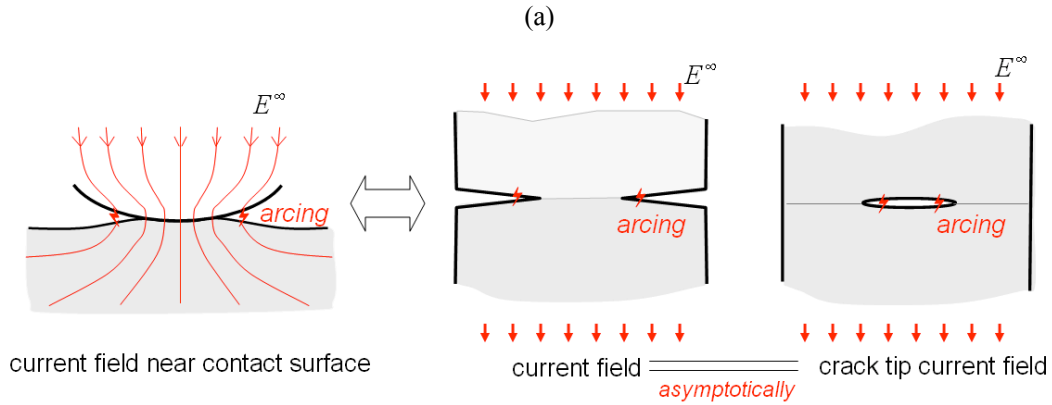
Contact vs Crack: Electrical Analogy

(b)

Fig. 2 Multi-physics crack models for rail track/armature contact

As reviewed in [6], from the viewpoint of mechanical analysis there are certain similarity between elastic contacts and crack problems in linear elastic fracture mechanics. Illustrated in Fig. 2a is the stress distribution and associated singularity at the end of contact zone between a flat-bottomed stamp and a semi-infinite substrate, which are essentially the same as that in the problem of double edge cracked panel under tension but with an opposite sign. In fact, a flat contact surface is formed by many asperities with the scales from nanometers to microns. According to the well-known JKR theory, at microscale the adhesion between contact surfaces becomes significant, which introduces

additional term to the classical Hertz's stress distribution with singularities at the ends of the contact zones of asperities. These singularities also possess the same structure as that in crack problem. These similarities provide the theoretical background to apply the crack model on the right hand side of Fig. 2a to analogy the stress distribution caused by the armature/rail track contact at macro and microscales.

Inspired by the crack/contact similarity in mechanical analysis, a step forwards achieved in this research is a developed crack analogy model of the electric current field for armature/rail track contact, as illustrated in Fig. 2b. The theoretical background of this analogy is based on the mechanical similarity between contact and crack as well as the coincidence between the two-dimensional Maxwell equations of static electromagnetic problems and the governing equation for mode III crack problems. The ongoing research proves that this kind of similarity also exists for dynamic problems under steady-state electrical pulse.

The proposed crack models on the right hand sides of Fig.2a or 2b play duel roles in this research: beside imitation of the contact phenomena, they also characterize the responses of the micro and macro cracks in materials under electromagnetic and mechanical loads, respectively. The threshold of the crack growth actually governs the fatigue life of the railgun track.

Hence, the crack model analogous to contact provides the distributions of electric current density, stresses and temperature near the edges of discontinuities such as contact surface. These distributions define the driving forces to the initiation and growth of the actual cracks located in these local areas.

The problems addressed by the crack models on the right hand side of Figs. 2a and 2b can be described as the boundary-value problem showing in Fig. 3, where a conductor with electric conduct coefficient σ^C contains an ellipsoid inclusion with dielectric coefficient ε_1. In this diagram, μ and v are Young's module and Possion's ratio, respectively; symbols *E, J, D, H, B* denote the macroscopic electric field, current density, electric displacement, macroscopic magnetic field, and magnetic induction field. All symbols and variables associated with the ellipsoid inclusion are denoted by subscription "1". The primary governing equations for this class of problems are the Maxwell equations and the momentum conservation at each material point whereby the Lorentz force presents as body force. The solution strategy introduced in this report is following these described in [9-15]
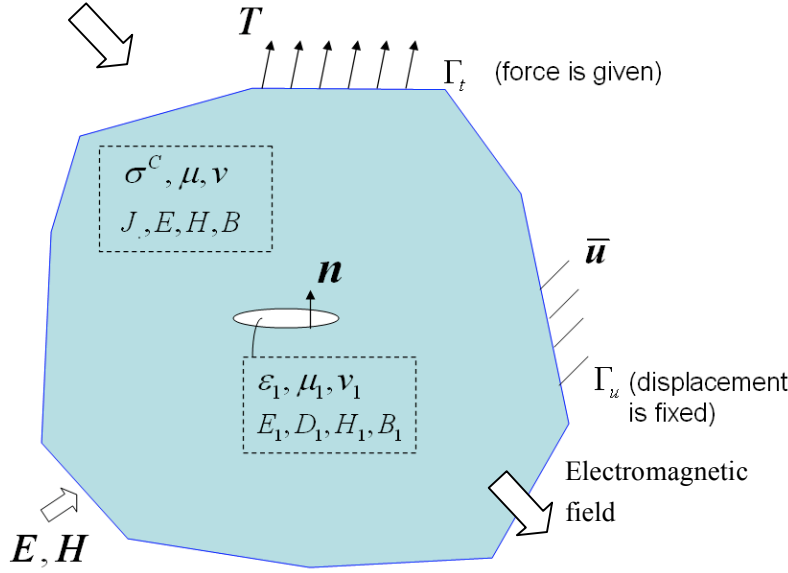
Fig. 3   A conducting solid body containing a dielectric cavity under a constant uniform remote electric intensity field as well as force and displacement boundary conditions, where ε, μ, v are the dielectric coefficient, Young's module and Possion's ratio, respectively. Corresponding

3 Mechanical, Thermal, Electrical and Magnetic Solutions for the Crack Model

In the theoretical analysis only the two extreme cases: plane stress and plane strain, are taken into account. For many engineering applications, they actually define the two extreme ends of all three dimensional structures, so the corresponding solutions provide the estimates of the upper and lower bounds of solutions in general. Preliminary three-dimensional numerical analysis has also been performed for the peel-off process of the lubrication layer on rail track surface.

Based on the crack model in Fig. 2a and 2b, researches have been performed focusing on the four issues: (i) strategies and technique for the theoretical analysis coupling electrical and magnetic load; (ii) macroscale field solutions of a crack in conductor governed by Maxwell's equation, momentum conservation and heat conduction equation; (iii) microscale solution and length scales. (iv) two and three dimensional numerical analysis. The configurations of solved specimen and major conclusions will be given in the following subsections. Detail derivations and formulations of theoretical solutions can be found in [8].

3.1 General Solution of the Magnetic Field Associated with Electrical Current

Regarding the first issue, it has been proven that the magnetic field solution is the conjugate function of electrical potential if no external magnetic field exists; which means, once the electrical field solution is well-known, the associated magnetic field can be solved easily through Cauchy-Riemmann's equation and the electrical potential.

This conclusion can be stated precisely as: for two-dimensional conductors and dielectric solids
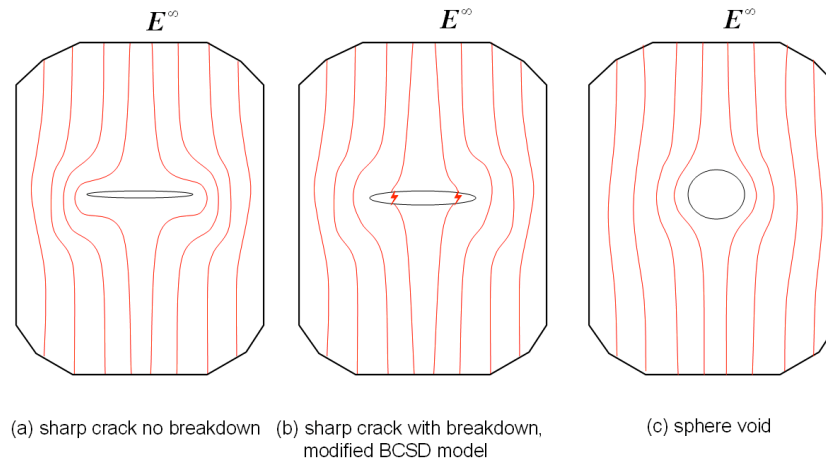
27

with electrical current but no extra external applied magnetic field, the solution to the quasi-static Maxwell's equations can be expressed as an analytical function in a complex plane in general. The real part of this analytical function equals the electric potential with minus sign and the imaginary part is the product of a constant and the magnetic field corresponding to the electrical current field solution, when conductivity is constant and Hall effect is omitted
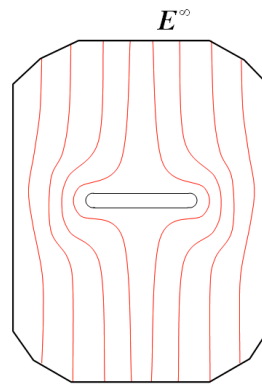
3.2 General Solution of the Magnetic Field Associated with Electrical Current

Four groups of analytical solutions have been obtained, which are (i) exact solutions of electric field, magnetic field, and Lorentz's force field for a central cracked infinite plane under a constant electric current at remote without electric-breakdown at crack tip (Fig. 4a); (ii) exact solution of electric field based on a proposed "modified BCSD model" for electric-breakdown (Fig. 4b); (iii) exact solution of electric field for a spherical void under a constant electric current at remote (Fig. 4c); the superposition of (i) and (iii) defines an approximate solution of blunted notch shown in Fig. 4d; and (iv) an analytical solution of temperature field based on a proposed asymptotic crack tip melting zone model (Fig. 4e).
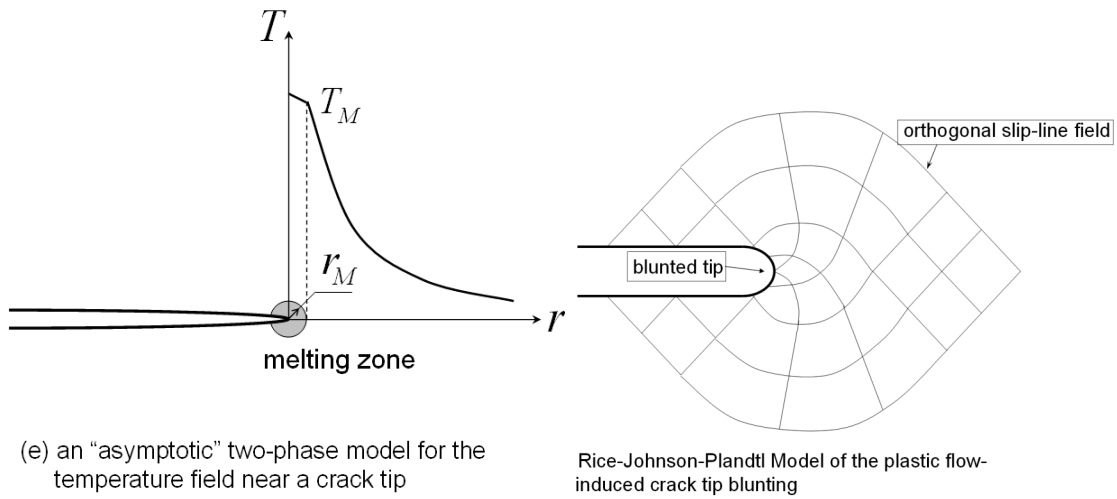
As illustrated in Fig. 5, the theoretical solutions reveal that the singularity of electric field exists at sharp crack tip, which leads to a concentration of energy dissipation with localized melting at the crack tip. As a competing mechanism, electric-breakdown removes this singularity. When there is no external magnetic field and mechanical load, the Lorentz force induced by the magnetic field associated with electric current field may cause remarkable stress intensity factor, which drives crack opening and possible subsequent propagation since either electric-breakdown or energy dissipation-induced melting will significantly reduce material's capacity against crack propagation. A quantitative discussion about the dominant mechanism under this situation will be given in the next section.

Several engineering applicable predictions have also been obtained from these solutions, which include the asymptotic distribution of temperature field, the stress intensity factor caused by electromagnetic load, and the thresholds of the remote applied electric field when breakdown and/or crack tip melting take place.


E^∞ E^∞ E^∞

(a) sharp crack no breakdown   (b) sharp crack with breakdown,   (c) sphere void
                                      modified BCSD model

28

(d) semi-analytical solution of
blunted notch: =(a)+(c)

(e) an "asymptotic" two-phase model for the
temperature field near a crack tip

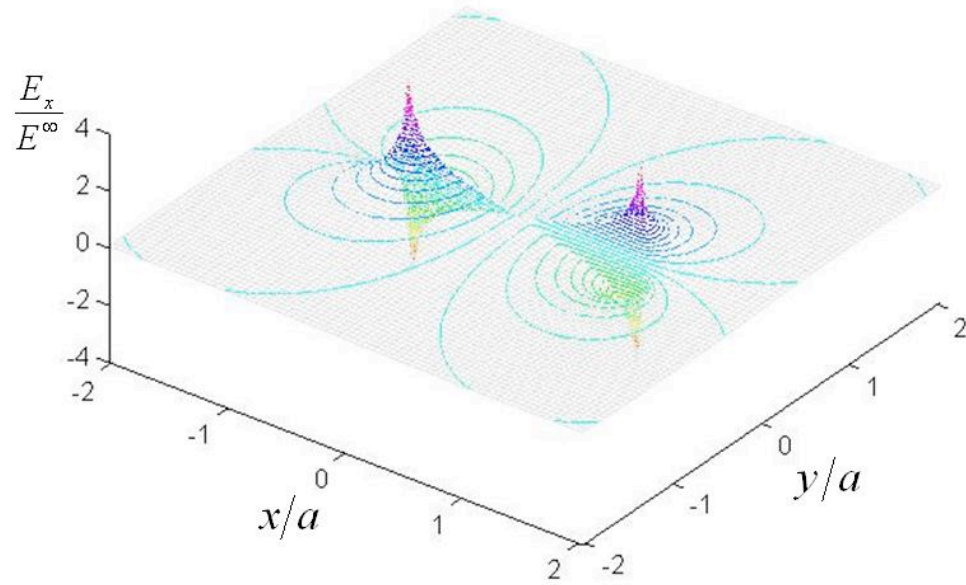Rice-Johnson-Plandtl Model of the plastic flow-
induced crack tip blunting

Fig. 4 The problems by which the analytical or semi-analytical solutions
have been found in this research, the details are given in [8].

29
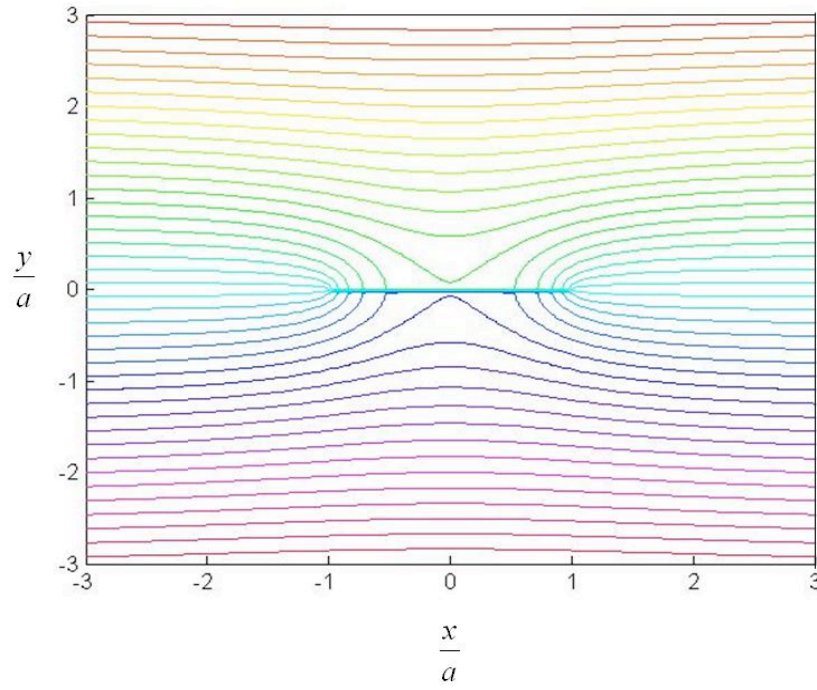
(a) The iso-valued contours of the total electric potential computed for the problem depicted by Fig. 4a
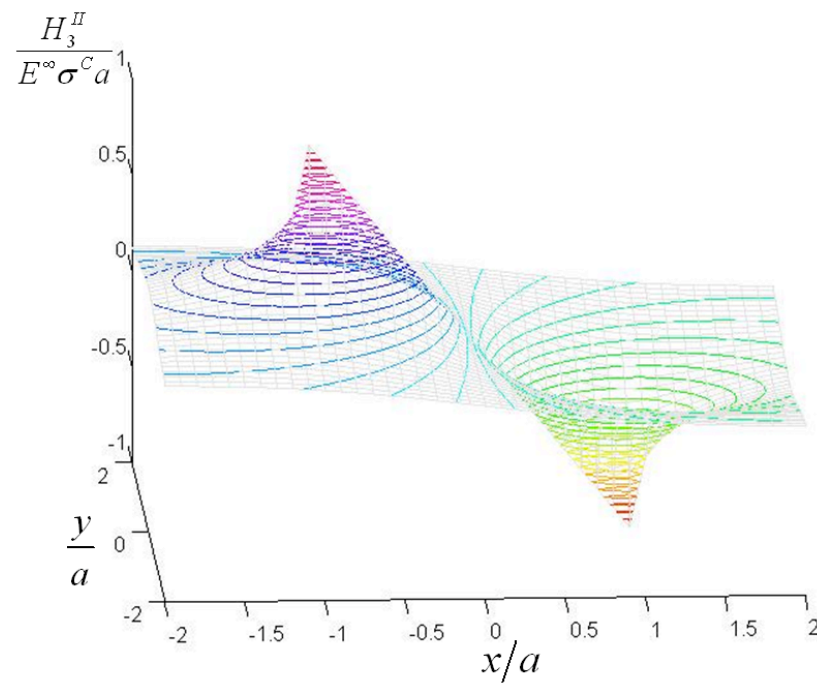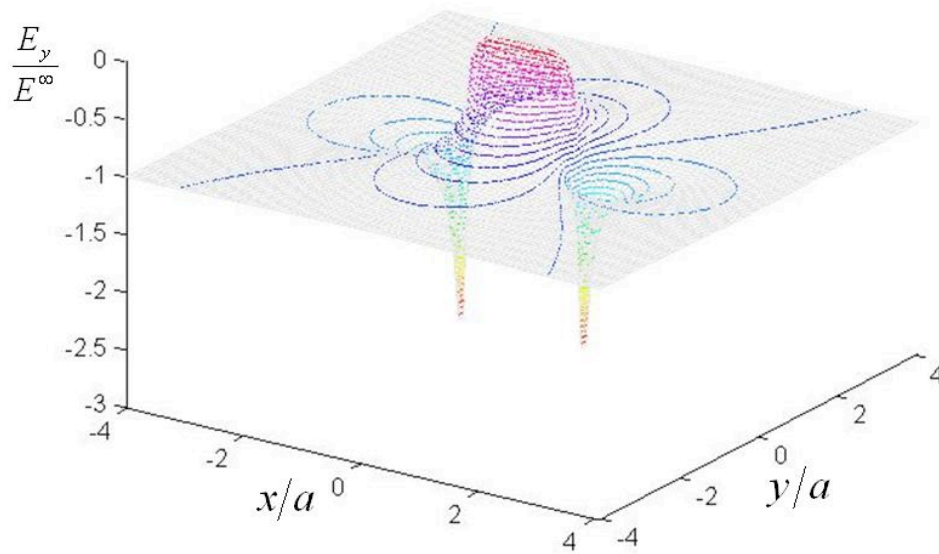

(b) The local magnetic field for the problem Fig. 4a

(c) Amplitude of the electric field in the x direction for the problem Fig. 4a, which has singularities at

$$|x| = a, y = 0$$

(d) Amplitude of the electric field in the y direction for the problem Fig. 4a, which is zero along the

line $|x| < a, y = 0$ but has a singularity at $|x| = a, y = 0$

Fig. 5   Solution to the plane problem of Fig. 4a.

31

3.3 General Solution of the Magnetic Field Associated with Electrical Current

Applying the semiclassical theory of conductors the elastic collisions between electron and impurities have also been studied. Solutions for three kinds of impurities: screw dislocation, solution misfited atom and an empty, have been obtained under the assumption of diluted distribution. The solved mean free path of electron, which is in the order about micron, defines the length scale that leads to the "threshold" of applied electrical load when a melting zone presents at a sharp crack tip.

3.4 Numerical Analysis

The theoretical studies for the problems illustrated in Fig. 4a-4d are focused on the effects of electrical and magnetic load when no external magnetic field applies. The crack solutions obtained are for the configurations made of single material system. Based on the experimental observation, e.g. [3, 4], numerical study has also been performed for the biomaterial system as illustrated in Fig. 1 when external magnetic field presents. As an ongoing research, the preliminary computation has been conducted for the two extreme cases that the current flow directions are perpendicular and parallel to the biomaterial interface, respectively. Depicted in Figs. 6 and 7, the two materials divided by the interface surface have different electrical conductivity, i.e. $\sigma_2^C \neq \sigma_1^C$, but with the same values for all other material's constants. The electrical potential with the fixed difference that equals the length of the specimen has been imposed to its two ends.

On the right hand side of the Fig.6 are the contours of the electrical field density and temperature increment caused by the electrical resistance induced dissipation. As expected, the part with higher conductivity is corresponding to less energy dissipation. the and the stress in horizontal direction. A magnetic field with the only non-zero unit component coincides to the unit outer normal of the plane has been applied on the specimen in Fig 7 with the ratio $\sigma_1^C / \sigma_2^C = 0.5$. On the right hand side of this figure are the contours of the computed electrical density, temperature increment caused by the electrical resistance induced dissipation, and the stress in horizontal direction. Since the voltage(electric potential) difference between the two ends of the specimen is fixed, the high conductivity part is with higher current flow and, more, higher energy dissipation and Lorentz' force. Plotted in Fig. 8 are the changes of the mode I and II stress intensity when the σ_1^C / σ_2^C varies. This plot provides the hint about how to adjust the mismatch in electric conductivity or the direction of magnetic field to the interfacial strength of the interface surface between lubricate layer and matrix material. A plot of the 3D peel-off simulation is also presented as Fig. 9.
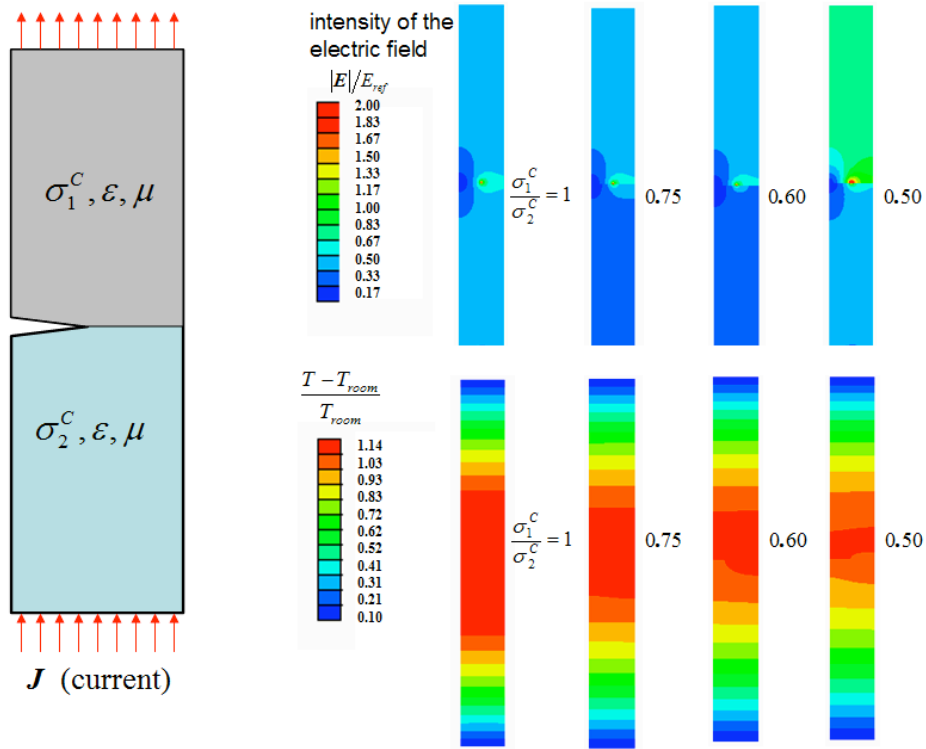
Fig. 6 Computational example of the case with the material mismatch only in electrical conductivity, the current flow direction is perpendicular to the interface.
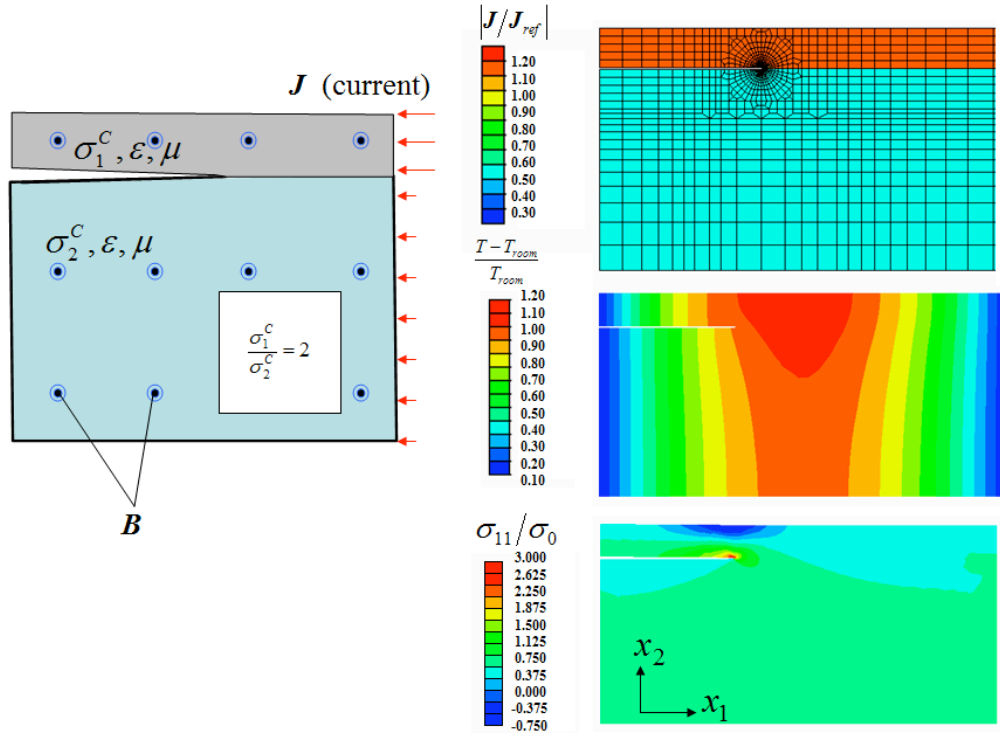
Fig. 7 Computational example of the case with the material mismatch in electrical conductivity, the current flow direction is parallel to the interface.
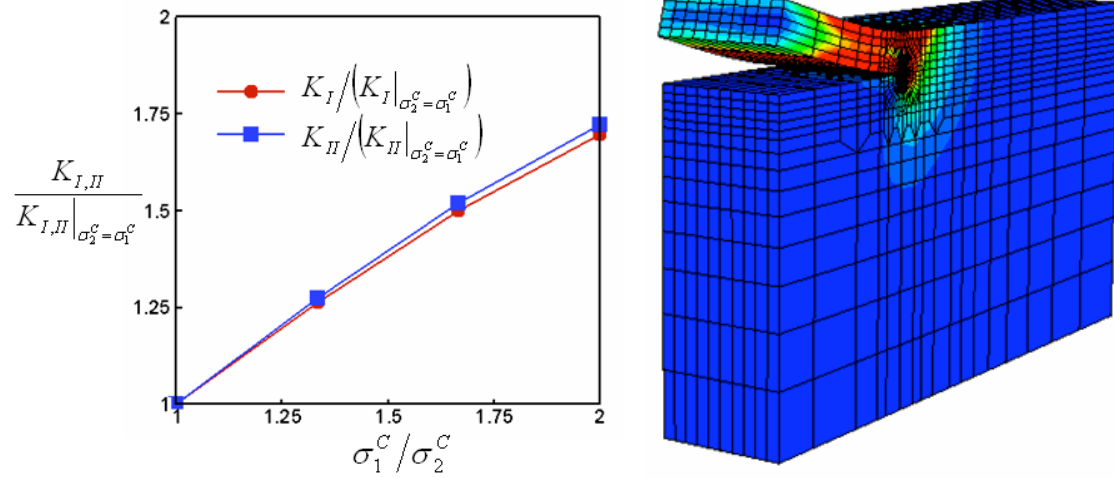

Fig. 8 The effect of conductivity mismatch on peel-off driving force

Fig. 9 A computational example of the peel-off

4. Two Competing Mechanisms: Breakdown vs Crack Tip Melting

4.1 The comparison factor D_p

The solutions and analysis described in the previous section reveal that the electric-breakdown and melting are the two most possible mechanisms to cause material's failure. An electrical circle model has been developed to identify the dominant mechanism among them, which is plotted in Fig. 10.
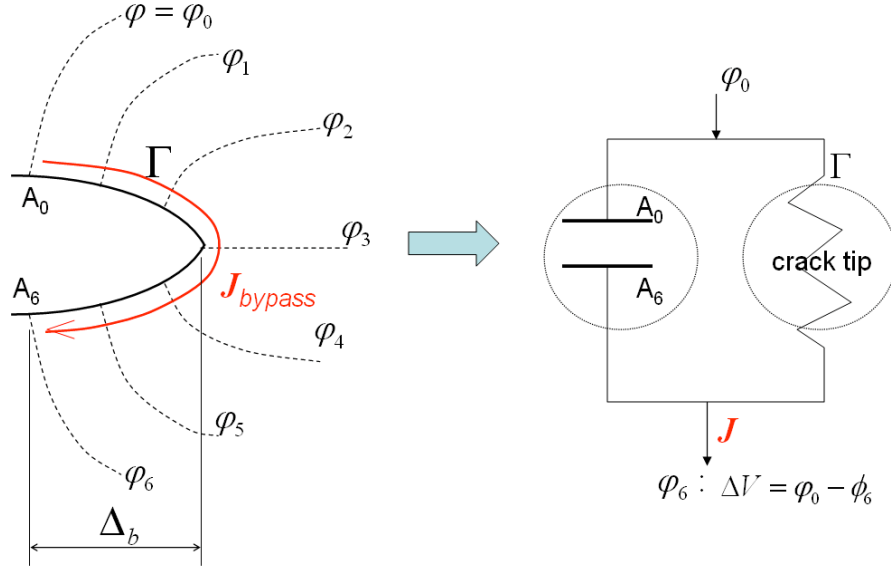

Fig. 10 A circle model that represents two competing mechanisms around a crack tip: the current breaks through the capacitance unit $A_0 A_6$ or goes bypass the crack tip.

Considering the material point pair (A_0, A_6) plotted on the left hand side of Fig. 10, which sits on the opposite surfaces near a crack tip with a potential difference, $\Delta V_{06} = \varphi_0 - \varphi_6$ (refers to Fig. 5(a)). This potential difference may drive electric current flowing through two possible ways: the path bypasses around the crack tip and the path breaks the air barrier between A_0 and A_6 by arcing. These two competing mechanisms can be simplified as the capacitance/resistance circuit model for a given current. A comparison factor D_p, defined as the ratio between the energy dissipations along these two possible current flowing paths, has been suggested to distinguish the dominant mechanism:

$$D_p = \frac{\Delta\Psi_{bypass}}{\Delta\Psi_{breakdown}} \tag{1}$$

35

Obviously, when the D_P defined by (1) is greater than unit, electrical breakdown dominates whereas the melting mechanisms takes over when $D_P < 1$, which provides a hint for the design of materials or devices with desirable governing mechanism.

Based on the theoretical solutions obtained, the comparison factor D_p can be expressed as the function of materials constant:

$$D_p = \frac{\Delta \Psi_{bypass}}{\Delta \Psi_{breakdown}} = 3\pi \sqrt[4]{8} \frac{\widetilde{G}^{\frac{3}{2}}}{\hat{g}^{\frac{1}{2}} \cdot \widetilde{H}} \log\left(\frac{\widetilde{\beta}}{16\hat{g}\widetilde{H}} \right) \tag{2}$$

where

$$\widetilde{G} = \frac{1}{k_{B2}k_I v_\kappa} \frac{aG}{\sigma^C \mu_H}, \quad \hat{g} = \frac{\left(g\sigma^C\right)^2 a^3}{\beta}, \quad \widetilde{H} = H_f \rho_m k_D a^3 \tag{3}$$

and

$$k_D = 1, \qquad k_{B2} = 0.12509, \qquad v_k = 0.1815 \qquad \text{for} \qquad v = 0.3$$

where a is the length of the crack, G is shear Young's module, μ_H is magnetic permeability, ρ_m is density, H_f is the fusion enthalpy per unit mass, $\beta = \widetilde{\beta}\sigma^C$ and $\widetilde{\beta}$ is a dimensionless coefficient and $\widetilde{\beta} \approx 100$.

Listed in Table I are the material's constants of four widely applied conducting metals and the corresponding values of D_P. In the second row from the bottom one finds that $D_P > 1$ for the three nonferric metals (Ag, Cu, Al) as well as for the iron at the low ferric end; whereas $D_P < 1$ for the iron at high ferric end. This is because higher permeability μ_H results in larger Lorentz's force, which leads to bigger crack opening displacement and, subsequently, requires higher voltage at breakdown according to Paschen's law. Hence, one may conclude that for a cracked specimen made of low ferric metals, electric-breakdown may occur easily, triggered by existing defects like cracks.

36

On contrast, for the cracked specimen made of ferric metals with high magnetic permeability, or the specimen is under an external mechanical force and magnetic field, which causes higher "k_I"; crack tip melting and subsequent thermal induced materials softening may become the more favorite mechanisms.

It should be pointed out that D_P in the third row from the bottom of Table I is obtained by the "k_I" that is computed by the solution of for the problem in Fig.4a which is a crack in an infinite plate. For a cracked plate with finite size the corresponding value of k_I can be very different. We will discuss the geometrical and size effects in details in the next research report. In order to demonstrate this effect, the D_P for $k_I = 300$ and $k_I = 500$ are also calculated and listed in the last row of Table I.

Table I: Material's constants (at room temperature) and the comparison factor D_P

	Ag	Cu	Fe	Al
G(GPa)	75.8	110	193	62
$\rho_M\,(\dfrac{kg}{m^3})$	10500	8960	7870	2700
$\sigma^C\,(\dfrac{10^6}{\Omega\cdot m})$	63	59.6	9.93	37.8
$\beta\,(\dfrac{10^8}{\Omega\cdot m})$	63	59.6	9.93	37.8
g($\dfrac{10^8 V}{m}$)	1.1	1.1	1.1	1.1
$\mu_H\,(\dfrac{10^{-7} H}{m})$	4π	4π	300-50000	4π
$H_f\,(\dfrac{j\cdot 10^5}{kg})$	1.048	2.087	2.437	3.97
$C_P\,(\dfrac{j\cdot 10^2}{kgK})$	2.35	3.85	4.49	8.97
D_P $k_I = \dfrac{3-\kappa}{2}(equ.24)$ plane stress	$1.79\cdot 10^4$	$2.02\cdot 10^4$	$8.01\cdot 10^3 \sim 3.72$	$3.71\cdot 10^4$
D_P	1.08	1.21		2.24

$\left(k_I = 3*10^2\right)$ plane stress			$0.483 \sim 2.24 \cdot 10^{-4}$	
D_P $\left(k_I = 5*10^2\right)$ plane stress	0.5018	0.566	$0.225 \sim 1.04 \cdot 10^{-4}$	1.042

kg: kilogram mass; m: meter; V: voltage; t: second, j: joul; H: Henry; crack length "a" = 0.02m; the values of β and g are collected from [16]; all material's constants are in SI unit.

4.2 Paschen's Law and Thresholds of Electric Load

An occurrence of electric-breakdown also depends upon the properties of the dielectric medium confined by the crack surfaces of the conductor. This fact is represented by the coefficient $\widetilde{g}$

in (2) which is a function of the parameters β that defined by Paschen's law [17].

An electric-breakdown between two opposite crack surface may occur when the interband transportation of electrons, i.e. breakdown between electron orbits, takes place, which may ionize atoms by break or form new interatomic bands. A macroscopic breakdown usually is the result of the applied voltage-induced ionization of the dielectric medium filled in the crack. This complex process can be phenomenologically described by the Paschen's law through the following simple expression:

$$\Delta V_{breakdown} = g\delta \tag{3}$$

where g is a constant in the order of 10^2(V/μ) when δ is the gap size in the unit of micron (μ).

Considering a notch in a two-dimensional conductor, the gap size is

$$\delta(r) = \delta_0(r) + \delta_{COD}(r) \tag{4}$$

Where δ_0 is the initial distance between two surfaces of the notch and δ_{COD} is the opening displacement after interal/external load applies; r is the distance to the crack tip. For a mathematically "sharp" crack, e.g. the problems illustrated in Figs. 5a-d: $\delta_0 = 0$. δ_{COD} can be estimated by the mechanical solutions for these problems while the voltage difference between two surfaces of crack is given by the electrical solutions.

First consider this sharp crack case, the corresponding "threshold" of E^∞ at breakdown is:

$$E^\infty_{breakdown} = \frac{2\sqrt{2}A_0}{g}, \qquad A_0 = \frac{G}{v_\kappa k_I \mu_H \left(a\sigma^C\right)^2} \qquad (5)$$

When an additional mechanical load, e.g. a uniform stress σ^∞, applies; it results in additional crack opening displacement:

$$\delta(r) = \delta_{COD}\left(r, E^\infty\right) + \delta_{COD}\left(r, \sigma^\infty\right), \qquad \delta_{COD}\left(r, \sigma^\infty\right) = \frac{\sigma^\infty \sqrt{2ra}}{4G(1-v)} \qquad (6)$$

The corresponding "threshold" is:

$$E^\infty_{breakdown} = \frac{1 + \left[1 - \sqrt{2a}\,g^2 A_1 A_2 \sigma^\infty\right]}{gA_2}; \qquad (7)$$

where

$$A_1 = \frac{\sqrt{2a}}{4G(1-v)}, \quad A_2 = \frac{\left(\sigma^C a\right)^2 v_\kappa \mu_H k_I}{G\sqrt{2}}$$

For a notch with two parallel surfaces, i.e. constant $\delta_0 \neq 0$ in (7), and ended by a semi-cylinder circle with the diameter δ_0, in this study an estimate of the threshold electrical load has been obtained by the superposition of the solutions of Fig. 5b and 5d, which leads to:

$$E^\infty_{breakdown} = \frac{1}{A_2}\left[\left(2 + \bar{\delta}\right) + \frac{1}{\sqrt{2}}\sqrt{8 + 4\sqrt{2}\left(\sqrt{2} - gA_2\right)\bar{\delta} + 2\bar{\delta}^2}\right]; \qquad (8)$$

where

39

$$\bar{\delta} = \frac{\delta_0}{\sqrt{L_m a}} \tag{9}$$

and L_m is the length scale according to the analysis in subsection 2.3; which is in the scale of micron.

Also, threshold to initial melting of a crack tip is

$$E_{melt}^{\infty} = \sqrt{\frac{2 L_m \rho_m H_f k_D}{a \sigma^C}} \tag{10}$$

5. 3D Computational model.

First consider the magnetic field generated by the uniform electric current flowing in a rectangular conductor of thickness c_e, as shown in Figure 1. The width of the plate is a_e, and the length of the plate is b_e. The current is flowing along Y direction. The origin of the coordinates is placed at the center of the cuboid. The distribution of the magnetic field is derived following the method proposed by Babic and Akyel (2005).
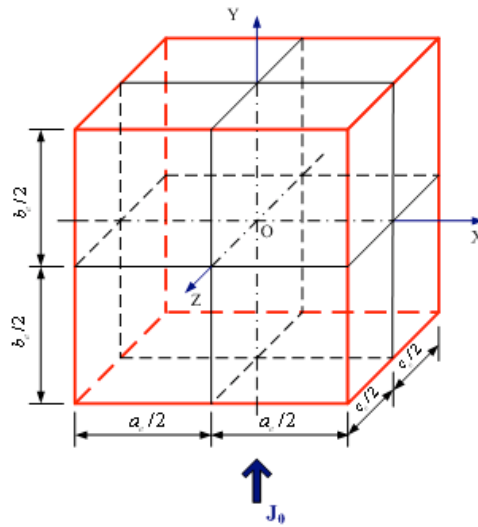

Figure 11 Conductive plate of dimension ($a_e \times b_e \times c_e$) subjected to uniform current $J_o \vec{j}$

By introducing the following auxiliary function

$$\lambda(x,y,z) = -x \cdot \arctan \frac{yz}{x\sqrt{x^2+y^2+z^2}} + \frac{y}{2}\ln\frac{\sqrt{x^2+y^2+z^2}+z}{\sqrt{x^2+y^2+z^2}-z} - \frac{z}{2}\ln\frac{\sqrt{x^2+y^2+z^2}-y}{\sqrt{x^2+y^2+z^2}+y} \quad (11)$$

the magnetic field is given by

$$H_z = \frac{J_0}{4\pi}\sum_{\alpha,\beta,\gamma=1,2}(-1)^{\alpha+\beta+\gamma}\lambda(x_\alpha,y_\beta,z_\gamma) \quad (12)$$

where

$$\begin{cases} x_1 = x - a_e/2 \\ x_2 = x + a_e/2 \end{cases}, \quad \begin{cases} y_1 = y - b_e/2 \\ y_2 = y + b_e/2 \end{cases}, \quad \begin{cases} z_1 = z - c_e/2 \\ z_2 = z + c_e/2 \end{cases} \quad (13)$$

Similar expressions can be developed for H_x due to $J_o\vec{j}$, and H_z and H_y due to $J_o\vec{i}$. It is noted that the above elementary solution is valid for any point inside or outside the plate. The numerical value of the magnetic field is finite everywhere, even at the corners of the plate.

The 3D numerical computation is performed on a large plate of thickness h containing an elliptic hole with major semi-axis a and minor semi-axis b. The distribution of the current density in the plate is evaluated. The computational domain is discretized into rectangular grids and adaptive mesh is used in the calculation. Each element size is determined so that the electric current can be regarded as uniform within the element. Numerical results for the magnetic field in the first quadrant are reported here. Results in other quadrant may be deduced by noting the symmetry argument: H_x is an even function of x and y, but an odd function of z; H_y is an odd function of x, y, z; and H_z is an even function of y and z, but an odd function of x. It can therefore readily conclude that both H_x and H_y vanish in the middle plane ($z = 0$), which agrees with the assumptions in the preceding 2D analysis.

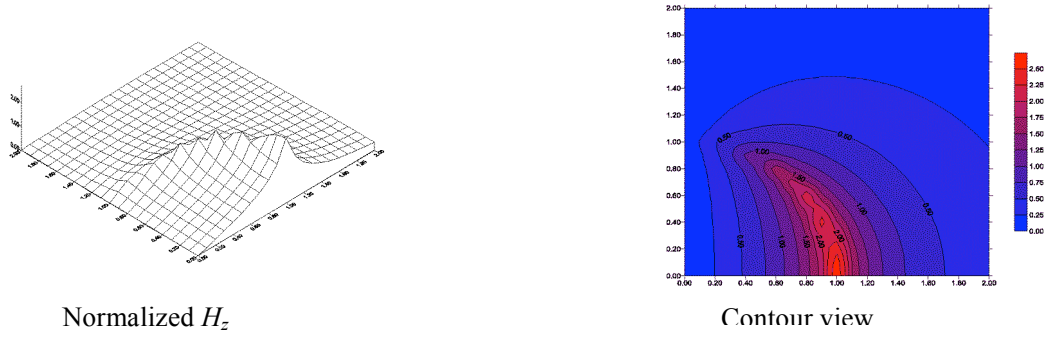Normalized H_z Contour view

Figure 12. Normalized H_z on the middle plane for $a/b=1$

The numerical results of H_z on the middle plane for $a/b=1$ are shown in Fig. 13. The thickness of the plate is $h/a=0.2$. Here and thereafter, all the magnetic components are nondimensionalized by a factor of $J_0 a/4\pi$.

On the top or bottom surface of the plate ($z=\pm h/2$), however, the 2D assumptions are violated, since H_x and H_y do not vanish, as illustrated in Fig. 4.
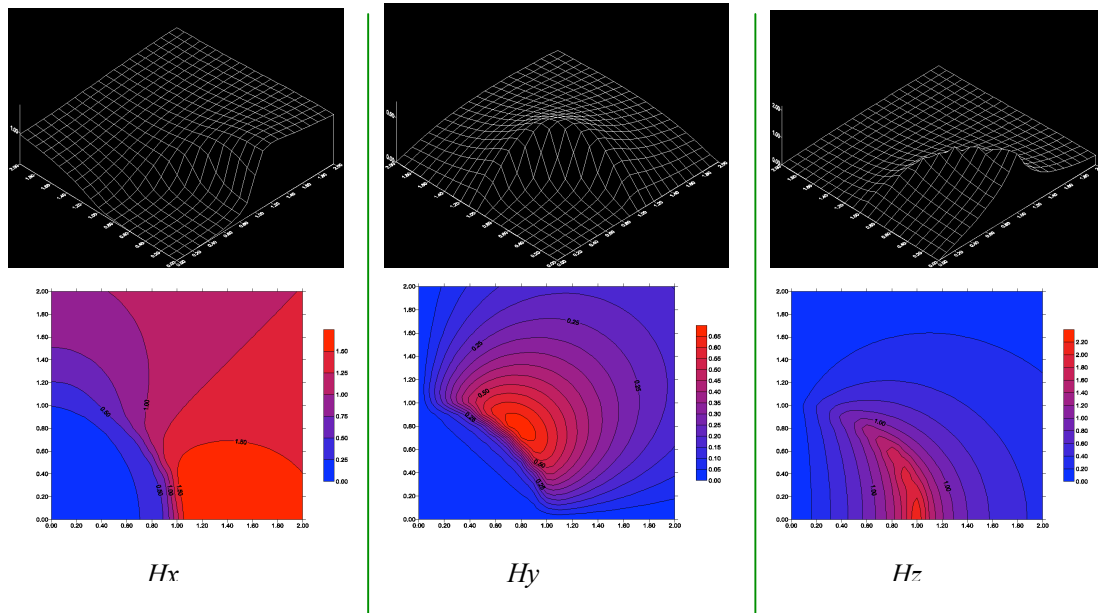

H_x H_y H_z

Figure 13. Normalized H_x, H_y, H_z on the top surface for $a/b=1$

42

The numerical results by the 3D computational model also show that unlike the 2D assumption, H_z also varies along the thickness direction of the plate. The figure below compares the variation of H_z along the *x*-axis on both the top and middle plane.
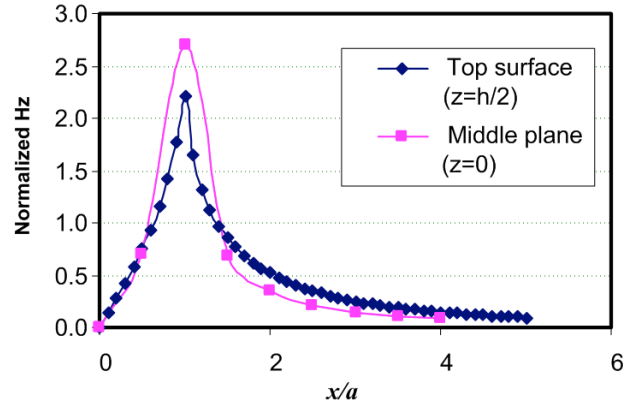

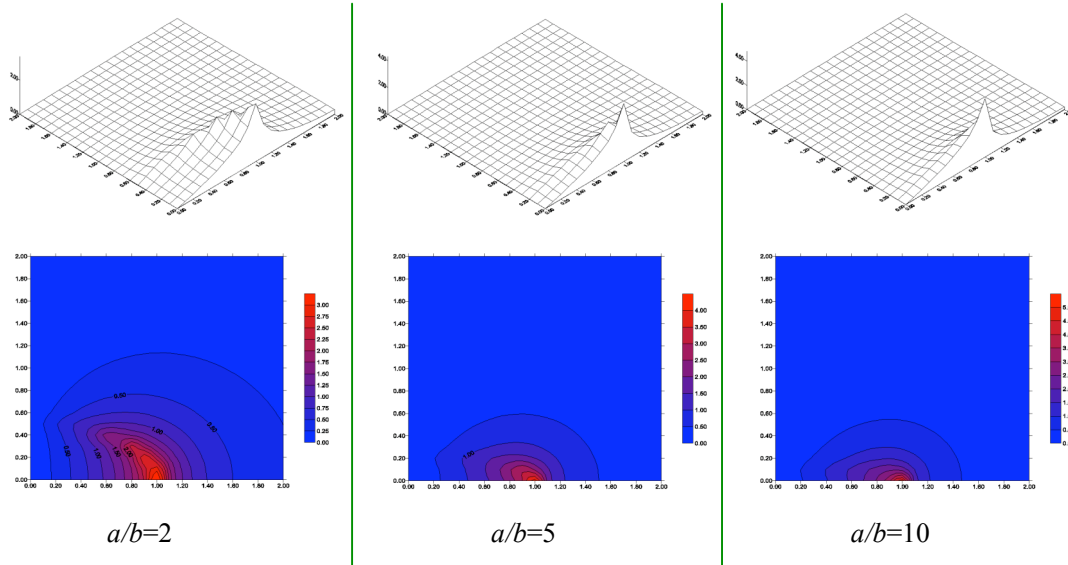Figure 14. Comparison of H_z between the middle plane and the top surface for $a/b = 1$

| a/b=2 | a/b=5 | a/b=10 |

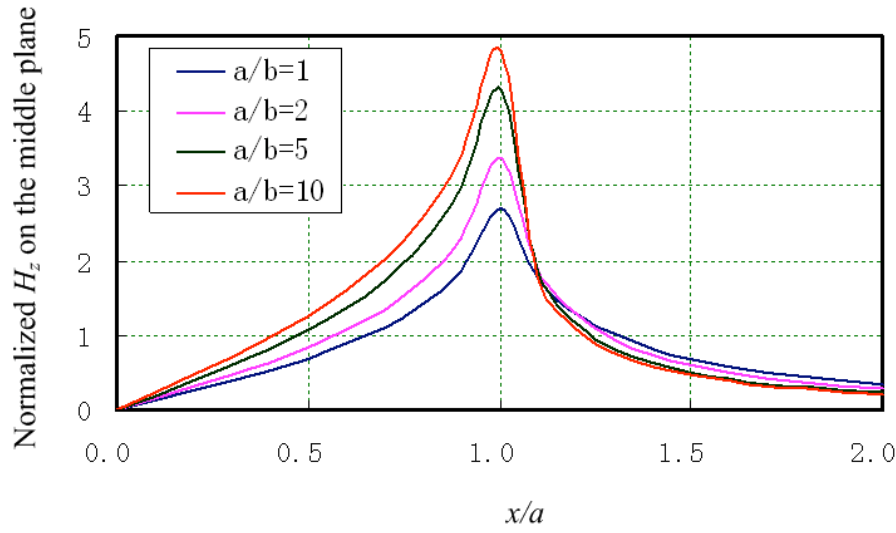Figure 15. Comparison of H_z at the middle plane for various *a/b*

43

Figure 16. Comparison of H_z along the x-axis at the middle plane for various a/b

Numerical computations are also performed for various ellipses with different eccentricities. Figure 6 illustrates the variation of the normalized magnetic component H_z along the middle plane. The disturbed zone becomes smaller as the ellipse becoming shallower. From Fig. 7, it is seen the maximum H_z indeed occurs at the vertex of the ellipse. This maximum value also becomes larger with decreasing b. In the case $a/b = 10$, the magnetic fields H_x, H_y, and H_z on the top surface are displayed in Fig. 8. The 3D numerical results show that the prevailing magnetic component in the plate is H_x when away from the elliptic hole.
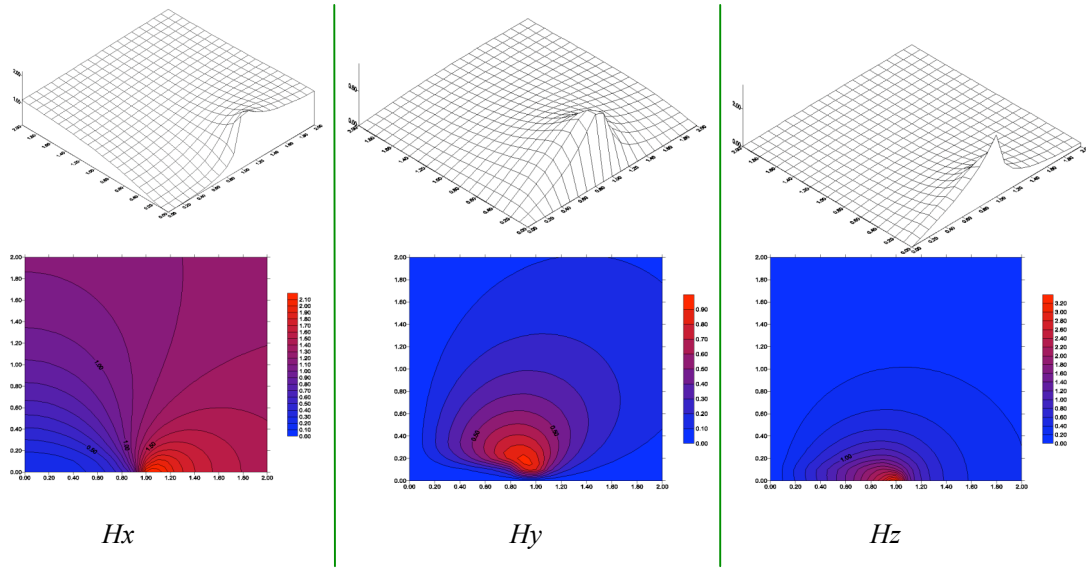
44

| *Hx* | *Hy* | *Hz* |

Figure 17. Normalized H_x, H_y, H_z on the top surface for $a/b = 10$

5. Conclusions

This study starts at the Lorentz' force and electric-breakdown in a conductor with defect such as a crack under electric load. The Lorentz force is induced by the magnetic field corresponding to electric current when no other external field applies, which may cause remarkably high stress intensity factor that results in crack opening and growth. In order to quantitatively identify the conditions for electric-breakdown and subsequent material's failure, close-formed mean field solutions near the crack tip have been obtained through solving Maxwell's equations, momentum conservation, and heat conduction equation. Under the framework of semi-classical theory of metals, mean free path and the interactions between electron and impurities have also been discussed.

The obtained solutions, in conjunction with the Paschen's law, define a threshold of applied electric load and associated energy dissipation that represents a "fracture toughness". By comparing the energy dissipations of the two competing mechanisms: a comparison factor D_p has been defined, which provides the possibility to quantitatively design of the rail track and armature materials with desirable governing mechanism that could bring up optimized strength, fatigue life and other mechanical, electromagnetical properties.

Appendix: Publications and Manuscripts in Preparation

Manuscript submitted and related publication:
[a07] "*Electromagnetically Induced Crack Opening Force and Condition for Electric-Breakdown I: General Solutions*", by S. Hao, Q. Wang, L. M. Keer; in review

45

[b07] "*Rolling Contact Between Rigid Cylinder and Semi-Infinite Elastic Body with Sliding and Adhesion", by* S. Hao and L. M. Keer. J. Tribology, 2007. **129**: p. 481-494

Manuscripts in preparation:

[c07] "*Electromagnetically Induced Crack Opening Force and Condition for Electric-Breakdown II: Dynamic Cases and Solutions for the Specimen with Finite Dimensions",* by S. Hao, Q. Wang, L. M. Keer , 2007

[d07] "New Material Constant to Characterize the Behavior of Bimaterial Contact and Crack under Electromagnetic Load – Especially W-W_xC_y and W-Cu systems" by S. Hao, Q. Wang, L. M. Keer , 2007

Remark: In the 2006 Annual Report the following two manuscripts were planed

[a06] "Transient Solutions of Skin-Effect and Electro-Magnetic-Induced Crack Driving Force", 2006
[b06] " Electro-Magnetic-Induced Crack Driving Force: Static Solutions", 2006

where the [b06] is actually the single solution depicted in Fig. 4a. As described in this report, the manuscript [a07] listed above includes the thermal, mechanical, electrical and magnetic solutions for the configurations plotted in Figs. 4a-4f. The [a06] will be a section of the manuscript [c07].

References:

1.   Keer, L.M., et al., *Simulation of Wear Particle Creation in Asperity Contacts Using the Finite-Element Method.* Tribology Transactions, 1993. **36**(4): p. 613-620.

2.   Liu, G., Q. Wang, and S.B. Liu, *A three-dimensional thermal-mechanical asperity contact model for two nominally flat surfaces in contact.* Journal of Tribology-Transactions of the Asme, 2001. **123**(3): p. 595-602.

3.   Persad, C., et al., *On the nature of the armature-rail interface: Liquid metal effects.* Ieee Transactions on Magnetics, 1997. **33**(1): p. 140-145.

4.   Satapathy, S., F. Stefani, and A. Saenz, *Crack tip behavior under pulsed electromagnetic loading.* Ieee Transactions on Magnetics, 2005. **41**(1): p. 226-230.

5.   Brown, L., et al., *Coefficient of friction measurement in the presence of high current density.* Ieee Transactions on Magnetics, 2007. **43**(1): p. 334-337.

6.   Hao, S., Keer, L. M., *Rolling Contact Between Rigid Cylinder and Semi-Infinite Elastic Body with Sliding and Adhesion.* J. Tribology, 2007. **129**: p. 481-494.

7.   Fine, M., Stolkarts, V., L. Keer *Fatigue crack nucleation assisted by thermal activation.* Materials Science and Engineering A-Structural Materials Properties Microstructure and Processing, 1999. **272**(1): p. 5-16.

8.   Hao, S., Wang, Q., Keer, L. M., *Electromagnetically Induced Crack Opening Force and*

46

Condition for Electric-Breakdown I: General Solutions submitted for publication, 2007.

9.   Laudau, L.D., Lifshitz, E. M. and Pitaevskii, L. P., *Electrodynamics of Continuous Media*. Vol. 8. 1960: Pergamon Press.

10.   Jackson, D., *Classical Elastodynamics*. 3 ed. 1975.

11.   Mushelishivili, N.I., *Some Basic Problems of Mathematical Theory of Elasticity*. 1953, Groningen. Holland.

12.   Rice, J.R., *Dislocation Nucleation from a Crack Tip* J. Mechanics and Physics of Solids 1992. **40**(2): p. 239-271.

13.   Eshelby, J.D., *Elastic inclusions and inhomogeneities* in *Progress in Solid Mechanics*, I.N. Sneddon, Hill, R., Editor. 1961, North-Holland: Amsterdam. p. 89-140.

14.   Ashcroft, N.W., Mermin, N. D., *Solid State Physics*. 1976, Fort Worth: Saunders College Publishing.

15.   Hoffman, C.A., et al., *Semimetal-to-Semiconductor Transition in Bismuth Thin-Films*. Physical Review B, 1993. **48**(15): p. 11431-11434.

16.   Slade, P.G. and E.D. Taylor, *Electrical breakdown in atmospheric air between closely spaced (0.2 mu m-40 mu m) electrical contacts.* Ieee Transactions on Components and Packaging Technologies, 2002. **25**(3): p. 390-396.

17.   Paschen, F., *Ueber die zum Funkenuebergang in Luft, Wasserstoff and Kohlensaeure bei verschiedenen Druecken erforderliche Potentialdifferenz (in German)*. Weid. Annalen der Physick, 1889. **37**: p. 69-75.

[18]   Babic, S. I. and Akyel, C. (2005). An improvement in the calculation of the magnetic field for an arbitrary geometry coil with rectangular cross section. International Journal of Numerical Modelling-Electronic Networks Devices and Fields 18(6): 493-504.

2.2 Application of Photonic Doppler Velocimetry Diagnostics in railguns

Investigators: Dr. Sikhanda Satapathy (512) 232-4455, sikhanda@iat.utexas.edu, and Dr. Scott Levinson

Technical objective: Use the Photonic Doppler Velocimetry to measure launch package motion inside the railgun accurately.

Technical approach:

Photo-Doppler Velocimetry (PDV) is a new technique that uses a heterodyne method and has many of the advantages of both the VISAR and Fabry-Pérot systems, while avoiding most of the disadvantages of both systems[4] [Strand et al., 2006]. The PDV at IAT is being custom built from commercially available parts and funded by DURIP for studying start-up behavior of armatures, and measure inbore kinematic characteristics of the launch package.

Progress statement summary:

Accurate velocity measurement in a one meter long railgun has been done. Techniques have been developed and tested for simultaneous measurements from breech and muzzle sides. These measurements have quantified the role of friction near the startup region.

Progress:

In FY2007 procurement of the PDV system is being carried out. In the meantime, a custom built system has been borrowed from National Securities Technology, Los Alamos for immediate use. The PDV technique provides excellent temporal and spatial resolution in measurement for full flight of the launch package in the laboratory railguns. The PDV method measures the minute Doppler shift in the monochromatic light reflected from the moving surface. The velocity of the moving surface is directly proportional to the Doppler shift in frequency. Off-the-shelf components developed for the telecommunications industry are used rendering the system robust and inexpensive. Solid state Erbium fiber laser producing 1550-nm light is used along with high-bandwidth optical detectors, high-sample-rate digitizers, and fiber optic circulators. The Doppler-shifted laser signal is mixed with the un-shifted signal to generate a beat signal. Short-time Fourier analysis of the beat signal produces highly resolved and accurate velocity profiles. The velocity, v is directly proportional to the Fourier peak of the beat frequency, Δf. Thus, $v = \lambda \, \Delta f / 2$.

Many of the initial applications of PDV have involved measurement of transient velocities (0-5 km/s) in shock-environments for relatively short times (< 500 µs) over short distances (< 0.2 m.) We have extended the utility of this method to obtain accurate velocity measurements over significantly longer time (> 10 ms) and longer distance (> 5 m.) The velocity is resolved within 0.05 m/s in 4 µs time

---

[4] O. Strand, D. Goosman, C. Martinez, and C. Whitworth, Rev. Sci. Inst. **77**, 83108, 2006.

intervals for the entire travel (including the free flight to target tank.) Simultaneous PDV measurements of the breech and muzzle probe signals of a 1-m EM launcher with projectile velocities reaching 350 m/s have shown very good agreement with each other, as shown in figure-1. Additionally, this optical technique doesn't suffer from the error arising out of shift in magnetic center in B-dot velocity measurements. Micro-retro-reflective surfaces are attached to the leading and trailing edges of the armature to reflect the Doppler shifted signals directly back to the respective probes. This ensures that reflected signals are insensitive to small changes in the respective normal angles due to armature balloting.
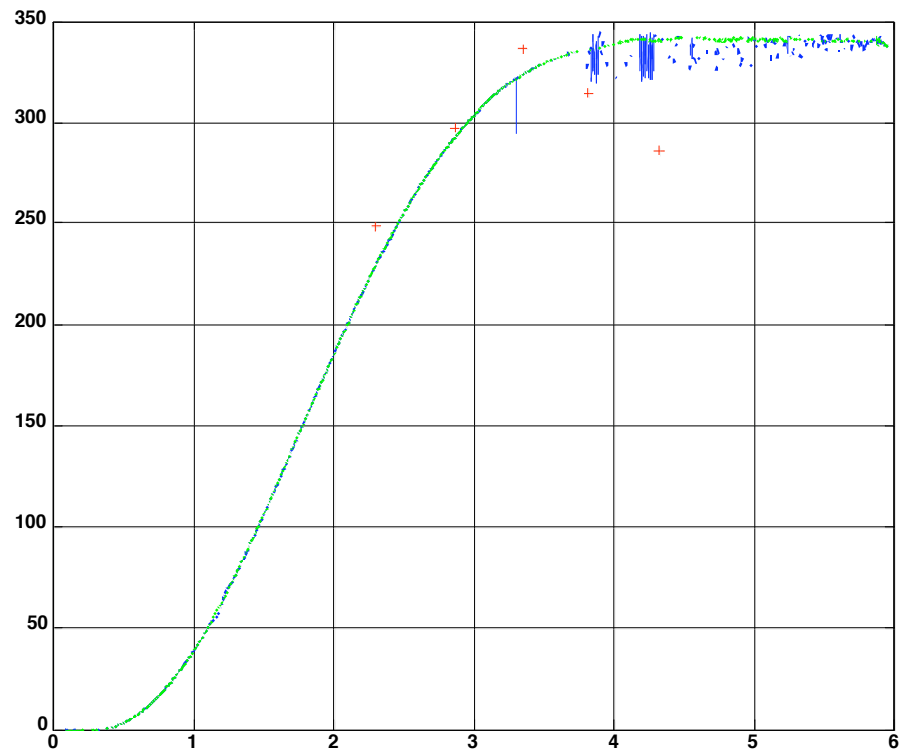

Figure 1: Velocity measured from breech and muzzle sides showed excellent agreement with each other. The B-dot data had showed deceleration due to shift in magnetic center, which doesn't affect the PDV measurement.

Publication:

S. Satapathy, et. al., "Measurement of friction in railguns using Photonic Doppler Velocimetry." ASME McMat Conference, Austin, TX (2007.)

49

2.3 Railgun Systems Level Bond Graph Model

Investigators: Michael D. Bryant, (512) 471-4870, mbryant@mail.utexas.edu

Technical Objectives: Construct and refine a railgun system model for simulation, to predict operation, understand system level interactions, permit scaling of guns to larger size, interpret diagnostic measurements, and aid design of future railguns.

Technical Approach

Approach involves identifying important components and physical effects in a railgun, constructing physics models of each component or effect, converting physics models into bond graph graphical models, integrating component models into a system model, extracting differential equations from the bond graph, simulating the equations on computer, and numerical investigation of operation.

Progress Statement Summary

Accomplishments for Fiscal Year 2007 include adding to the railgun system model:

- Skin effect in rails: The constitutive law was based on a ladder circuit of 4 resistors and 3 inductors. This circuit is consistent with observed frequency (to 30 kHz) dependence of rail resistance and inductance. This circuit contains the dependence of rail resistance and inductance on rate of current (di/dt). Skin effect had significant influence on simulations, with losses and reduced inductance reducing the effective inductance gradient L'.
- Velocity skin effect at armature and rail, formulated as a velocity dependent constriction resistance in the armature and the rail-armature interface. Velocity skin effect influenced system simulations.
- Effect of containment structure on gun propulsive force, via eddy current losses in the magnetic response of the containment structure.
- Addition of transverse forces between armature and rails, including
  o Magnetic pressure
  o Contact generated forces
  o Magnetic blow-off forces
  o Elastic response of rails
- Conversion of Mathematica program into matlab code, for future use by railgun users.

Progress

Simulations of railgun model now include the following subsystems and effects:

- capacitor bank power supply, with switching,
- rail resistance and inductance influenced by skin effect,
- rail-armature interface influenced by mechanical contact, velocity skin effect, and contact resistance,
- losses in containment structure
- longitudinal motion of armature and package

~ friction and drag forces on armature and package

Outputs of simulations match measured data of rail current, armature velocity, armature position, muzzle voltage, and breech voltage. As was reported earlier, contact resistance must still escalate with time, for simulations to match measurements.

<u>Publication</u>: A Bond Graph Model of Railgun Longitudinal Propulsion System, M. D. Bryant and R. Quintanilla, abstract submitted to 14th Electromagnetic Launch Technology Symposium.

<u>Supported</u>: Mahitha Kaliki, M.S. student, female.
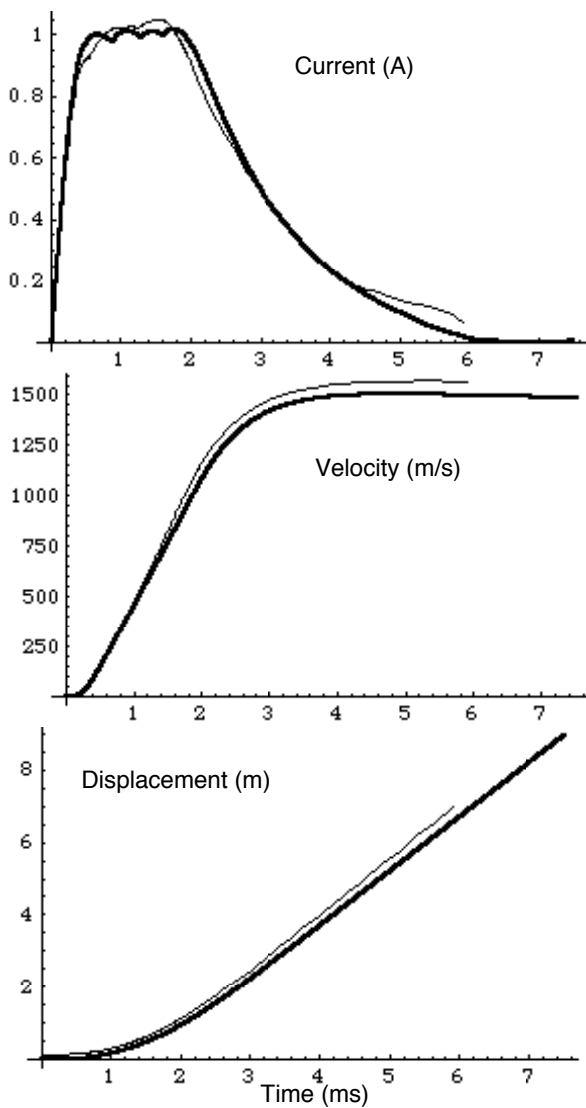
51

3.1 Developing the R/A Interface: R/A Contact and Lubrication: Fusible alloy lubrication of aluminum-aluminum interface

Personnel: G. Ghosh, M.E. Fine, Y.-W. Chung, and J. Wang, Professors
                       Peter Hseih, Graduate student

Technical objectives

The armature-rail contact in electromagnetic railgun launchers is characterized by high sliding velocity and current density. The high current density and operating temperature at these contacts complicate the challenge of minimizing electrical resistance while avoiding severe wear and friction at the sliding interface. The dilemma posed by the competing electrical and mechanical demands may be avoided through the use of liquid metal lubricants, as suggested by several authors [1] [2]. The melting of aluminum armatures during launch supplies liquid metal to the interface, but the liquid aluminum causes undesirable metallurgical reactions with copper rails [3] and is a source of transfer film porosity [4]. Investigation of melt lubricants with lower melting points has not been reported previously. The present study examines the effect of Ag-Bi, Bi, Bi-In, Bi-Sn, and Sn melt lubricants with different armature reservoir geometries on the launch efficiency and tribology of aluminum armatures on aluminum rail cladding over the course of a 5-shot series.

Technical approach

Low melting-point alloys were cast into reservoirs on the end of 6061 Al pins for use with a CTEC high temperature tribotester. A fixed load of 5.0 N was applied to the pin as it rotated against a polished 6061 Al disk at 0.8 mm/sec. The coefficient of friction was calculated from the friction force on the pin.

Aluminum armatures were machined at Northwestern University's Prototype Lab with shallow and deep reservoirs from 6061 Al stock. Melt-lubricant alloys were cast directly in the reservoirs. The armature faces were then machined flat and ground to an interference fit with sandpaper. The benchtop railgun at IAT Labs was lined with 3003 Al cladding. The cladding surface was cleaned with isopropyl alcohol prior to launch. Armatures were launched with a charge voltage of 225 V, with an average peak current of 80 kA. A Rogowski coil was used to record the current profile as a function of time. Six b-dot sensors were used to measure the position of the armature as a function of time. The position data was used to calculate armature velocity. The recovered armatures were weighed to determine launch mass. The effective inductance gradient was calculated for each launch based on the armature mass, current, and peak velocity. The cladding was removed following each 5-shot series and marked with rail polarity. A fresh set of cladding was used for each melt-lubricant.

Progress statement summary

Melting of Bi-In was observed to decrease the coefficient of friction in a pin-on-disk test configuration for 6061 Al. Introduction of fusible-alloy melt lubricants helps to maintain an effective inductance gradient of 0.41 μH/m over a 5-shot series. The effect is independent on the composition or melting point of the lubricant. In the absence of a melt lubricant, the effective inductance gradient of the control armatures decreased from 0.38 to 0.29 μH/m. This may be due to cladding wear and the loss of of a good interference fit between the armature and cladding. Tapered aluminum armatures maintain an effective inductance gradient of 0.40 µH/m.

Progress

Eight 5-shot series have been completed on the IAT benchtop railgun. The results of these tests are summarized in figure 2 and figure 3. Direct measurement of the effective inductance gradient of the benchtop railgun indicates a value of 0.532. All of the armatures had values below the direct measurement value. Transfer films were observed for all lubricated shots.
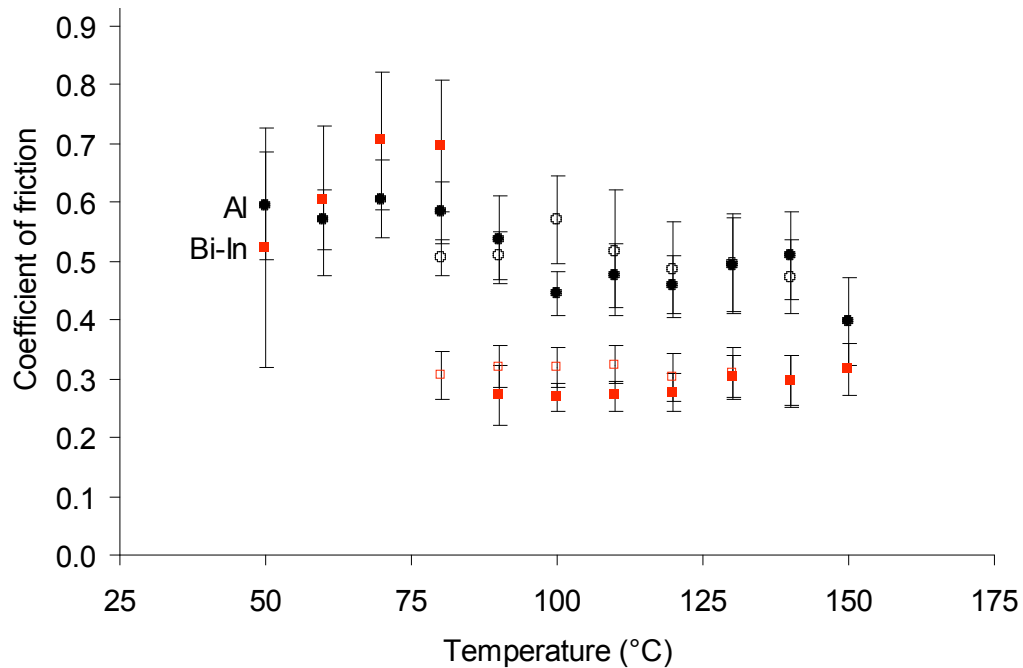

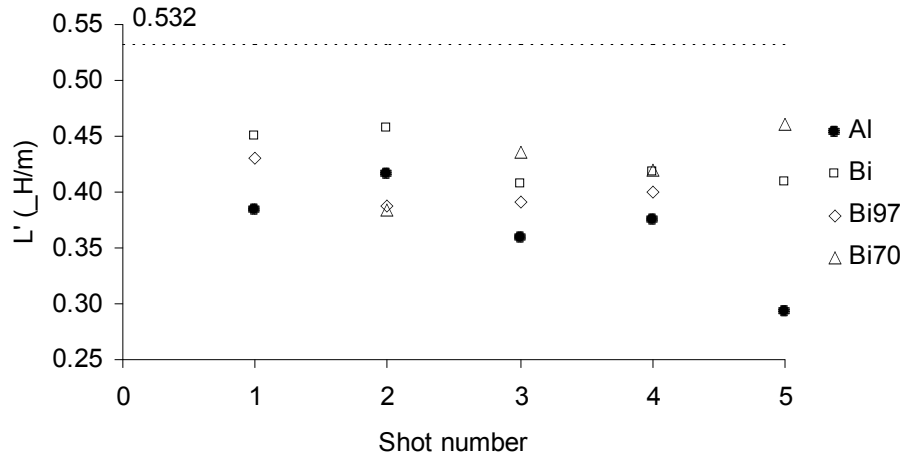**Figure 1**: Bi-In melt lubrication of 6061 Al

Figure 2: Effect of Ag-Bi composition on effective inductance gradient
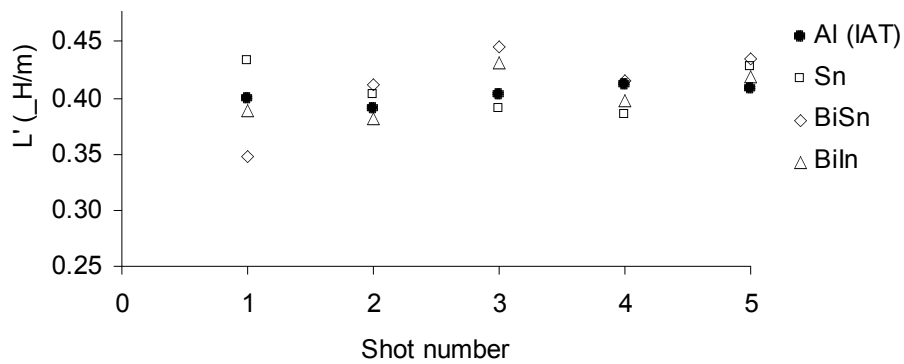

Figure 3: Effect of melting point on effective inductance gradient

References

1. Drobyshevski, E.M., E.N. Kolesnikova, and V.S. Yuferev, *Calculating the liquid film effect on solid armature rail-gun launching*. IEEE Transactions on Magnetics, 1999. **35**(1): p. 53-58.

2. Salant, R.F. and L. Wang, *Simulation of liquid lubricant injection in electromagnetic launcher armatures*. IEEE Transactions on Magnetics, 2007. **43**(1): p. 364-369.

3. Persad, C., *Railgun tribology - chemical reactions between contacts*. IEEE Transactions on Magnetics, 2007. **43**(1): p. 391-396.

4. Persad, C. and Z. Castro, *Railgun tribology: characterization and control of multishot wear debris*. IEEE Transactions on Magnetics, 2007. **43**(1): p. 173-177.

54

3.2 Role of Electrical Skin Effects and Current Crowding on the Stability of Armature-Rail Contacts in Railguns

B. Lead: University of Texas at Austin

C. Principal Investigator: Indranath Dutta, Naval Postgraduate School, Ph: 831-656-2851, E-mail: idutta@nps.edu

D. Report Period: 1 August 2005 - July 15 2007

E. Statement of Objectives:

The objective of the project is to obtain fundamental insight into the role of high electrical current on the development of microstructural damage at the armature-rail contact, the rail surface, and in the armature, with emphasis on the role of current crowding and electromigration-related effects.

F. Background and Research Goals

Although it is qualitatively known that current crowding occurs near the rear corners of the armature-rail contact, the metallurgical effects of current crowding on rail/armature damage has not been studied. Furthermore, although armature-melting is known to result in damage to the rails, the details of rail-damage mechanisms and their relation to current crowding are not well understood. Finally, the influence of polarity on Al-melt deposition on rails is unknown. These issues are addressed here.

G. Accomplishments

G1. Effect of current crowding on microstructural evolution at rail-armature contacts (FY 2006)

The microstructures of armatures fired with and without applied current in a dual-armature railgun were analyzed. A distinct. localized Joule heat affected zone (JHAZ) with graded microstructures was noted in the current-carrying armature. It was established that Joule-heating, as opposed to friction, is largely responsible for the initiation of armature melting. The location of the melt-initiation zone correlated well with the experimentally observed location of the melt-zone in the armature. The extent of current crowding was found to increase with increasing electrical contact conductance and decreasing electromagnetic skin depth in the rail. The results suggest that if current crowding can be minimized without raising contact conductance, localized melting can be substantially reduced, and therefore, rail damage can be mitigated. [1]

G2. Electric Current Induced Melt Movement on Cu Rails (FY 2007)

While conducting experiments on a model system to evaluate whether electromigration-related effects are significant in rail-armature systems, it was serendipitously discovered that molten Al is transported along the Cu rail under the influence of the applied electric field.

To understand the mechanism of liquid transport under an electric field, simple model experiments were conducted where a drop of Ga was placed on a stripe of thin film Cu on Si, and a current (4-7A) was applied along the Cu stripe, as shown in Figures 1a-d. Joule heating melts the Ga, which travels down the Cu stripe in the direction of the applied current, producing a Ga

coating on the Cu stripe. The location of the Ga melt front as a function of time was determined using voltage changes at specific locations along the Cu stripe (locations A-D in Figure 1e) . From this, the melt front velocity (v) was computed, and the activation energy Q for Ga movement along the stripe was determined. The measured Q of 17.35 kJ/mole is close to the activation energy for self diffusion in liquid Ga (~19 kJ/mole), suggesting that the flow of Ga along the Cu is diffusion-controlled. It was inferred that the *flow occurs by electromigration of Ga ion cores under the influence of the direct electrostatic force*, such that the direction of flow is from the positive to negative terminal. This is *opposite to the direction of conventional electromigration* in solids, which occurs under the influence of the electron wind force, from the negative to the positive terminal.

Similar experiments were also conducted to measure the kinetics of Al-melt transport along Cu rails using a model miniature stationary railgun. The results, summarized in Figure 2, showed that the activation energy of Al movement under the influence of the electric field equalled Q for diffusion in liquid Al, suggesting that the observed flow occurs due to electromigration of liquid.

G3. <u>Metallurgically Induced Rail Surface Damage Evolution during Firing : Cu/24Ag (FY 2007)</u>

The evolution of deposits on Cu/24Ag rails following multiple shots with 7075Al armatures were studied (Figure 3). The following features were observed: (i) a thin interfacial layer which was found to be roughly equiatomic Cu/Al, (2) a thick intermediate layer that is porous, Al and O rich, and which also has Ag, with oscillating O delineating the deposit from each shot, (3) a thin surface layer which is mostly O-rich Al, but sometimes comprised CuAl or AgAl; and which was also O-rich, and (4) the Cu-deposit interface was typically found to be smooth where the debris was undisturbed, but rough wherever the thick debris spalled off. This suggests that the following sequence of events occurs when multiple shots are fired from the same gun: (1) First, molten Al-Zn-Cu alloy is deposited on the rail; (2) then, Cu and Ag dissolve into melt; (3) oxygen dissolves into and/or reacts with the turbulent melt; (4) melt is hydrolyzed if moisture is present : $2Al +$

$3H_2O \rightarrow Al_2O_3 + 6\underline{H}$; (5) O and H react to form more H_2O (vapor); (6) as the melt cools, vapor

is trapped, creating porous layer which is rich in oxygen/oxide; (7) as the melt cools, Cu-Al

intermetallics form at the interface (CuAl; maybe $Cu_{11}Al_9$, $Cu_{33}Al_{17}$); (8) the brittle Cu-Al

IMC layer may break, and float up during successive shots; (9) during successive shots, the porous, oxygen/oxide rich Al layer grows thicker; and (10) finally, when thick debris layer spalls, rail damage occurs. It was inferred that in general, debris spallation is required for rail damage by gouging.
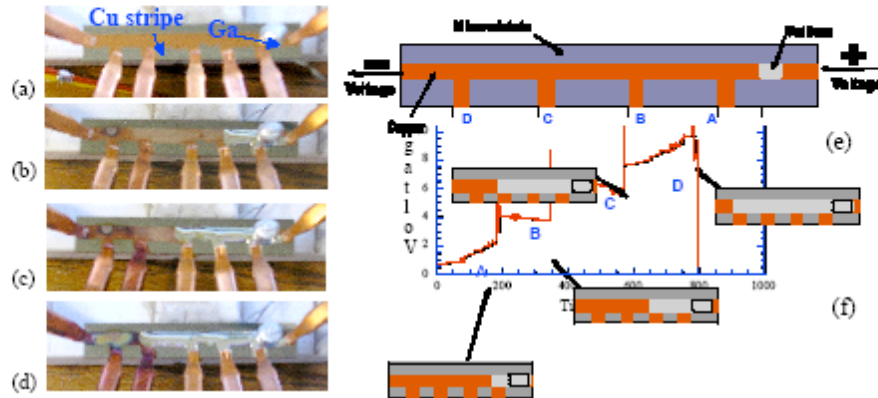
Figure 1: (a-d) Current-induced movement of Ga along Cu stripe; (e) sample schematic, showing voltage measurement points (A-D) along Cu-stripe length; (f) voltage trace showing location of Ga front as a function of time. Insets in (f) show location of Ga schematically.
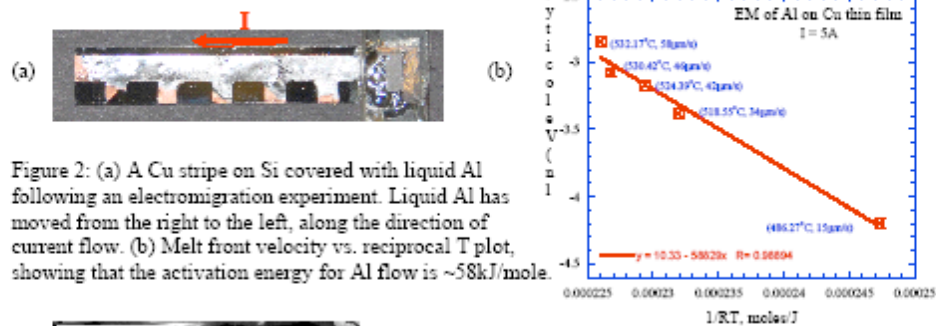

Figure 2: (a) A Cu stripe on Si covered with liquid Al following an electromigration experiment. Liquid Al has moved from the right to the left, along the direction of current flow. (b) Melt front velocity vs. reciprocal T plot, showing that the activation energy for Al flow is ~58kJ/mole.
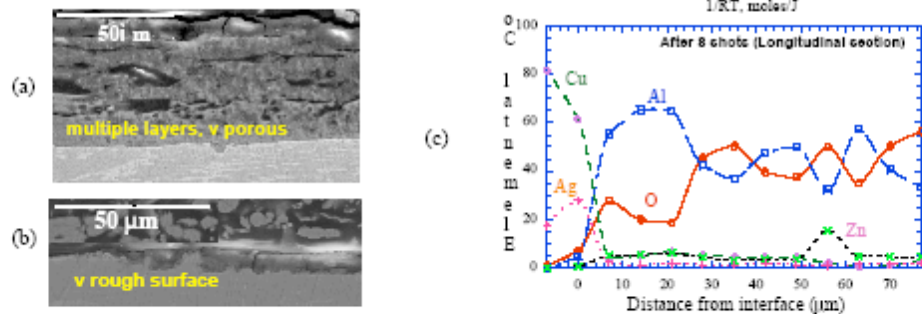

Figure 3: Micrographs of debris on Cu/24Ag rail after 8 shots, showing (a) a region with smooth rail-debris interface where multiple porous layers adhere to the rail surface, (b) a region where the rail surface has become very rough owing to spallation of the debris, and (c) through thickness composition of the debris showing that it comprises primarily of oxidized Al, with oscillating Al and O concentrations.

3

57